Hybrid femtosecond/picosecond coherent anti-Stokes Raman scattering for gas-phase temperature measurements of counterflow flames at elevated pressures

---

A

Thesis

Presented to

the faculty of the School of Engineering and Applied Science

University of Virginia

---

in partial fulfillment

of the requirements for the degree

Master of Science

by

Sean Alberts

December 2021

APPROVAL SHEET

This

Thesis

is submitted in partial fulfillment of the requirements
for the degree of

Master of Science

Author: Sean Alberts

This Thesis has been read and approved by the examing committee:

Advisor: Chloe Dedic

Advisor:

Committee Member: Harsha Chelliah

Committee Member: Christopher Goyne

Committee Member:

Committee Member:

Committee Member:

Committee Member:

Accepted for the School of Engineering and Applied Science:

Craig H. Benson, School of Engineering and Applied Science

December 2021

Abstract

Well-controlled laboratory experiments using reactors with canonical geometries, such as counterflow burners, can be used to evaluate the ability of chemical-kinetic mechanisms and transport properties to predict combustion processes. Although counterflow diffusion flames have been employed previously to explore the validity of chemical kinetic mechanisms near flame extinction, measuring temperature and local strain rate with sufficient accuracy to obtain validation data is a challenge. For this thesis, femtosecond/picosecond coherent anti-Stokes Raman scattering (fs/ps CARS), a laser-based spectroscopy technique, has been used to quantify gas temperature in a counterflow diffusion flame at atmospheric and elevated pressures.

To enable this study, a three-axis stage system was developed to translate the CARS measurement location relative to the flame while maintaining precise spatial and temporal overlap of the laser pulses utilized to generate the CARS signal. An additional challenge addressed was maintaining the stability of multiple beam positions over the 40 ft propagation distance between the laser system and the counterflow burner. The success of employing fs/ps CARS in large-scale combustion environments relies on mitigating alignment and stability challenges identified during this study. Methods used to align fs/ps CARS and improve system stability are presented in the current work.

To my parents.

Acknowledgements

I would like to thank the Department of Mechanical and Aerospace Engineering for providing the opportunity to pursue my education here at the University of Virginia.

I would like to thank my parents, Susan and Mark Alberts, without whom my life today as I know it would not be possible. Through the values they instilled in me, I have been able to accomplish much over the course of my life so far and will continue to do so under their loving guidance.

I would like to thank the rest of my family as well for their love and advice. Even as I droned on about my research, they would lend an ear and offer encouragement.

I would like to thank my roommates, friends, and girlfriend for their constant support throughout the duration of my time here. With their presence alone, I have been able to maintain my sanity and strengthen my resolve to stretch for a brighter future.

I would like to thank my advisor, Dr. Chloe Dedic, who enabled this opportunity to be possible. Despite my several shortcomings, her tutelage allowed me to grow as both a person and a researcher. Under her guidance, I was able to experience the birth of a new lab and grow alongside it. She always stuck beside me even during the rough moments, and for that I will be forever grateful.

I would like to thank Dr. Harsha Chelliah. I took over a portion of his lab space and his burner, and was never the best at organization, however, he continued to always offer his advice to me and always took an interest in my research. Without his support, I would not have been able to conduct the experiments presented in this thesis.

I would like to thank my various lab partners and research collaborators. Their support throughout the years helped guide and shape me as a researcher, and enabled me to experience the joys of working in a team. I would like to especially thank Dr. Clayton Geipel and Mr. Ryan Thompson for the multitude of hours spent assisting me.

I would like to thank the Virginia Space Grant Consortium New Investigator Program which funded in part the construction of the three-axis translation stage featured in this research.

Finally, I would also like to thank my thesis committee for their part in assisting move on with my life's journey.

Table of Contents

List of Tables

List of Figures

Chapter 1

Introduction

1.1 Motivation

Controlled combustion for energy production has proven to be a primary contributor to the rise of modern society. As of February 2021, the energy produced through the combustion of non-renewable fossil fuels is 60.3% of the total energy produced in the United States alone [2]. The combustion of fossil fuels have a plethora of harmful emissions that contribute to global warming. Methane, CH_4, a primary component of natural gas, is the second most abundant anthropogenic greenhouse gas and accounts for 20% of total greenhouse gas emissions [3]. CH_4 is extremely potent in trapping heat in the atmosphere, about 25 times as much as CO_2, but fortunately is relatively short-lived. As CH_4 is a potent but short-lived greenhouse gas, investigation of its chemical kinetics during combustion processes can inform how to mitigate its impact on the environment. Such investigations have already been reflected in the design of modern gas turbines.

To improve thermal efficiency and reduce fuel consumption, modern gas turbine engines are moving to higher operational pressures (50+ atm). In order to design optimal high-pressure turbines for a range of traditional and alternative fuels while minimizing production of harmful emissions, chemistry models must be accurate over the range of fuel and pressure conditions of interest. Well-controlled laboratory experiments using reactors with canonical geometries, such as counterflow burners, can be used to evaluate and improve existing chemical kinetic mechanisms and to better understand combustion behavior, including soot production, at high pressures [1]. Accurate and precise measurements of thermodynamic variables and species concentrations are needed to provide validation and inform the further development of such models.

In traditional flame studies, physical probes such as thermocouples and species sampling probes have been utilized to make measurements. However, measurements made using laser-based diagnostic tools have several advantages over those made with physical probes. Where traditional thermocouple measurements exhibit large errors due to conduction, convection, and radiation heat transfer, laser-based diagnostic tools do not disturb the chemical and fluid dynamics of the system being studied [1]. Furthermore, laser-based measurements are typically *in situ*- meaning the measurement occurs in the sample volume- and non-invasive. For example, particle imaging velocimetry (PIV) provides insight into the velocity of the flow being studied, laser-induced incandescence (LII) can inform the amount of soot being produced within a flame environment, and coherent anti-Stokes Raman scattering (CARS) spectroscopy can be used to measure temperature and species concentrations [1, 4, 5, 6]. Each optical measurement has advantages and disadvantages that should be considered before application. Some of these considerations include available optical access, pressure and temperature of the reacting flow being studied, spatial and temporal resolution required of the measurements, accuracy and precision desired, and cost and complexity of the full experiment.

1.2 Research Goals

This thesis presents the development and use of a fs/ps CARS system for thermometry of counterflow flames at atmospheric and elevated pressures. Spectra acquired in the products of a near-adiabatic flame using a Hencken burner will be used to validate spectral parameters input into a numerical model. This model will simulate the spectral response of N_2 at different temperatures. In addition, an electric field model for a sinc^2 ps probe will be implemented to compare simulated CARS spectra against experimental measurements using a library-searching algorithm to determine best-fit gas temperatures. Setup of a three-axis linear stage controller system will also be discussed to meet the requirement for spatial and temporal stability of the laser beams used for the fs/ps CARS process.

In summary, the goals of this research are:

1. Characterize the long-term spatial stability of the fs/ps CARS system to enable experimentation using the counterflow burner.

2. Develop a three-axis translational stage system to precisely control the location of the CARS measurement volume within a stationary counterflow burner.

3. Develop a numerical model to match the experimental probe pulse shape for use in the simulation of spectra.

4. Investigate temperature profiles of a diffusion counterflow flame across a range of pressures and strain rates using fs/ps CARS thermometry.

1.3 Thesis Outline

The remainder of Chapter 1 includes a brief introduction of theory and review of literature to introduce previous work using coherent anti-Stokes Raman scattering (CARS) spectroscopy and counterflow diffusion flames and to provide context for the current thesis. Chapter 2 details experimental setup, including the burner and development of the optical layout. Chapter 3 reports challenges encountered and addressed related to the stability of the fs/ps CARS system. Chapter 4 presents experimental fs/ps CARS measurements of an adiabatic flame and a counterflow diffusion flame at different pressures and strain rates. Best-fit temperatures are determined by comparing experimental results with spectral simulations employing a newly developed sinc^2 probe model, and temperatures are compared to 1-D flame calculations. Chapter 5 will conclude with a summary of research and future recommendations.

1.4 Literature Review

1.4.1 Counterflow Burner Geometry

While real-world combustion flow fields are generally complex and exhibit turbulence and dynamic fuel-air mixing, laboratory burner configurations can employ much simpler laminar flow field geometries to explore fundamental chemistry effects. Canonical burner configurations significantly simplify the experiment, allowing fluid effects, chemistry, and flame structure to be separately and accurately analyzed. Counterflow burners are one common canonical burner configuration, and counterflow diffusion flames having been studied extensively in both laboratory and numerical settings [1, 7, 5, 8, 9, 10, 11].

The counterflow configuration uses two nozzles aligned opposite of one another. Premixed and partially premixed combustion can be explored by using one nozzle to flow a mixture of fuel and oxidizer and the other to flow a dilute oxidizer or inert species, or an identical mixture of reactants [12]. Non-premixed combustion, the focus of the current thesis, can be achieved by flowing fuel and oxidizer through opposed nozzles [1, 13]. In addition to the main nozzles, many configurations also feature an annulus surrounding the fuel and oxidizer nozzles to flow an inert gas, typically N_2 or He, to serve as a shroud that assists in stabilizing the flame.

Both experimental and computational studies have been performed in counterflow diffusion flames to extract temperature, velocity, and species concentration with varying fuel/oxidizer compositions and for different flow conditions. Laminar counterflow diffusion flames are especially useful since they permit investigation of these features uncoupled from the effects of turbulence. Measurements of flame structure in turn allow validations of hydrodynamic models describing the flow field. They also allow refinement of transport properties and thermodynamic properties being employed in the evaluation of the hydrodynamic models. This is in part due to the relative ease in modeling the flame behavior as the the flow field can be accurately characterized through a one-dimensional similarity solution obtained from the solution to the Navier-Stokes equations for a flow impinging on a flat surface as developed by von Karman [11]. Additionally, as the flame is stabilized away from the nozzles it is much easier to solve for temperature and species as there is less uncertainty in the heat loss terms in the energy equation [7]. The impact of global strain rate on flame structure has also been explored. Strain rate can be defined as a function of inverse residence time and is related to the axial velocity in 1-D flame environments. Strain rate measurements have been used to inform aspects of combustion that are difficult to predict computationally [1, 13, 14, 7, 10]. For instance, soot production has been shown to occur at low strain rates as the rate of nucleation is directly tied to residence times within the flame. Another characteristic tied to strain rate is extinction as flow velocity impacts heat loss. The extinction of a flame is dependent on the chemical kinetics of oxididation and is not easily predicted numerically [15]. However, the kinetics of the reaction rate are dependent on the flame temperature, and thus accurate measurements of flame temperature made near extinction provides further insight into the kinetic mechanisms [16]. Though to perform these measurements, a diagnostic tool that does not interfere with the flame structure and ongoing chemical reactions is required. As such, laser diagnostics are the preferred tool for making non-invasive measurements. Temperature measurements have been made with a range of laser diagnostics, with the diagnostic chosen for the present work being coherent anti-Stokes raman scattering spectroscopy [17, 7, 18].

1.4.2 Coherent Anti-Stokes Raman Scattering Spectroscopy

For over five decades, coherent anti-Stokes Raman scattering (CARS) spectroscopy has been utilized to measure both temperature and species concentrations of major and minor species in combustion environments [19, 20, 21, 22]. CARS is a four-wave mixing spectroscopic technique that uses two electric fields, denoted pump and Stokes, to induce a Raman coherence for a Raman-active target

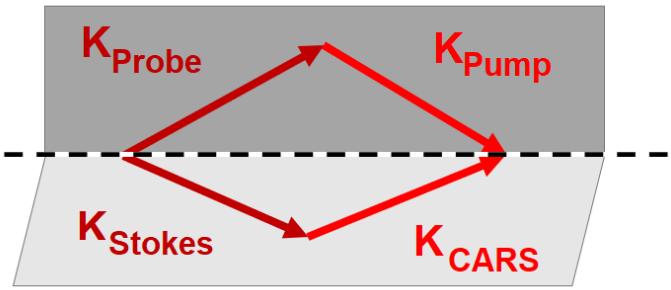

Figure 1.1: Folded BOXCARS phase matching layout.

molecule between molecular energy states. This coherence is subsequently probed using a third electric field generating a coherent laser-like signal at a blue-shifted frequency to satisfy the conservation of energy and momentum [23, 24, 25]. Each pulse can be described as a time-dependent electric field given by

$$E_i(\vec{r},t) = E_i(t)\exp[i\vec{k}\vec{r} - i\omega t] \tag{1.1}$$

where k is the wave vector along the propagation direction r, ω is the frequency, and $E(t)$ is the pulse envelope of the electric field [26]. The frequency of the generated radiation (the frequency of CARS), ω_{CARS}, is bound by the conservation of energy, and the phase matching of the four-wave mixing process is similarly bound by the conservation of momentum.

$$\omega_{pump} + \omega_{probe} - \omega_{Stokes} - \omega_{CARS} = 0 \tag{1.2}$$

$$k_{pump} + k_{probe} - k_{Stokes} - k_{CARS} = 0 \tag{1.3}$$

CARS occurs when the energy difference of the four-wave mixing signal is generated at the positive anti-Stokes wavelength. The individual pulses are termed pump, Stokes, probe, and CARS as shown in Eq. 1.2 and Eq. 1.3. A common phase-matching configuration for CARS uses crossed beams and is referred to as BOXCARS. Folded-BOXCARS, used in the current experiment, has advantages over traditional BOXCARS due to enhanced spatial resolution at the measurement volume and results in the CARS signal propagating in a direction separate from the other three beams, enabling spatial filtering of the CARS signal [6].

CARS can be used to make temperature and species concentration measurements in combustion environments [19, 16]. CARS spectroscopy is well suited for these measurements due to its direct

measurement of the temperature dependent population of vibrational and rotational energy states described by the Boltzmann distribution [19]. Therefore, the spectral structure is highly temperature dependent, while the relative amplitude of the signal originating from different Raman-active molecules is related to the concentration of the targeted species. Molecular nitrogen, N_2, is most frequently measured due to it being inert and its high concentration in air-breathing combustion [19].

Much of the current literature on CARS is centered around the use of nanosecond (ns) laser sources[22, 27]. Ns CARS has proven to be a robust technique capable of measuring temperature in harsh combustion environments such as the U.Va. supersonic combustion facility [28], and can make measurements with a reported accuracy of 2% [29, 30]. However, ns CARS has been observed to be susceptible to non-resonant background interference and is not collisionally insensitive, thus reducing accuracy and sensitivity in pratical combustion experiments performed at elevated pressures [31, 32, 33]. This limitation has been addressed through the implementation of polarization discrimination, which succeeded in reducing non-resonant background contributions but at the cost of a large reduction in the measured CARS signal. Additionally, the thick windows needed for high pressure applications can scramble the polarization of the CARS signal and reduce the effectiveness of this technique. However, with the development of ultrafast laser systems, this limitation can be addressed.

One of the primary advantages of using mode-locked ultrafast laser pulses for CARS thermometry is that unlike ns sources, fs laser pulses are generated by actively mode-locking an oscillator with a broad bandwidth. This allows frequencies to oscillate in phase, producing short, intense coherent signal with broad spectral content. This is followed quickly by destructive interference which allows for the temporal suppression of non-resonant background. This will be discussed in detail in Chapter 3.

The development of ultrafast laser systems in turn led to new variations of the CARS technique. Two such variations are broadly defined as femtosecond (fs) CARS and picosecond (ps) CARS. For a detailed explanation of fs CARS, the reader is directed to a paper by Lucht et al. that details the theoretical use and implications of the diagnostic [34] and a paper by Kearney et al. features it in experimental practice [35]. For applications and discussion regarding ps CARS the reader is referred to experiments conducted by Meyer et al. and Roy et al. [36, 37]. Both techniques have been shown to be capable of single-shot thermometry, however, each has shown to have unique advantages aside from temperature measurements. Ps CARS has been proven to have a high accuracy in measuring Raman linewidths in the time domain [38, 39], whereas fs CARS has been proven capable

of simultaneous excitation of mutliple species, such as N_2 and CO [40] and O_2 and CO_2 [41]. However, a novel approach was presented by Prince et al. [42] sought to combine the advantages garnered from the two techniques into a single cohesive diagnostic tool. This diagnostic came to be termed hybrid fs/ps CARS. For an exhaustive overview of the development and implementation of hybrid fs/ps CARS, the reader is directed to the dissertation of Prince [43] who helped develop the technique and the dissertation of Miller [23] who showcased some of the first experiments with fs/ps CARS for gas-phase thermometry.

Hybrid fs/ps CARS was first demonstrated by Prince et al. for condensed-phase and gas-phase species detection, but it was not until 2010 with Miller et al. [44] that it was used for gas-phase thermometry for the first time. Fs/ps CARS benefits from the spectral resolution and suppression of nonresonant signal of ps CARS and the broadband excitation of multiple transitions simultaneously of fs CARS. With higher peak energies and repetition rates than nanosecond (ns) CARS thermometry, hybrid fs/ps CARS provides the temporal (<100 ps) and spatial (approximately 1 mm x 100 μm) resolution needed to measure temperatures and species across the laminar reaction zone for a range of gas pressures and velocities [45, 46, 25, 23, 47, 48]. Hybrid fs/ps CARS in particular serves well for high pressure studies. The primary advantage offered by fs/ps CARS for flame studies at elevated pressure is that its signal is not susceptible to collisional quenching when short pulse delays are employed and, as a result, is relatively insensitive to pressure effects [49, 50].

Although the counterflow diffusion flame has been the target of several combustion studies, only a small subset have focused on utilizing fs/ps CARS to investigate temperature within this flame environment and even fewer have evaluated the effects of pressure on peak gas temperature for a flame near extinction [51, 52, 53, 7]. As such, this experiment seeks to use fs/ps CARS and apply it for quantifying temperature in a counterflow flame at elevated pressures and various strain rates.

Chapter 2

Experimental Setup

2.1 High-Pressure Counterflow Burner

This experiment utilizes a counterflow burner located at the University of Virginia Reacting Flow Laboratory to study methane/air diffusion flames at elevated pressures. A full description of the burner has been discussed at length by Sarnacki et al. [1, 54]. The counterflow burner used in this experiment features opposing jets of fuel and oxidizer and co-annular nozzles flowing nitrogen gas to shield the fuel and oxidizer in the inner flow. The jets are housed within a pressure chamber with a maximum operating pressure of 50 atm with optical access through fused silica windows on four sides [1].

Both the fuel and nitrogen nozzles are 6.5 mm in diameter with a set distance of 5.45 mm between the nozzles for the current investigation. A schematic of the burner is shown in Fig. 2.1. The burner has been previously run at pressures up to 30 atm with varying distance between the nozzles, so the studied pressure of 4 atm is well within the range for operation. For the pressures studied, N_2 dilution of the fuel was used to shift the location of the laminar flame towards the center line of the burner and to enable fs/ps CARS thermometry using N_2 across the full reaction zone. For pressures exceeding 8 atm, helium, He, dilution of both the oxidizer and fuel lines is necessary to maintain a laminar flame.

As shown in Fig. 2.2, the counterflow burner and the laser system are located in separate rooms. Routing optics and final steering mirrors are located in an adjacent room. Positioning of the CARS probe volume is executed using a breadboard supported by a three-axis translation stage system. Additional detail concerning the three-axis translation system will be covered in Chapter 3.

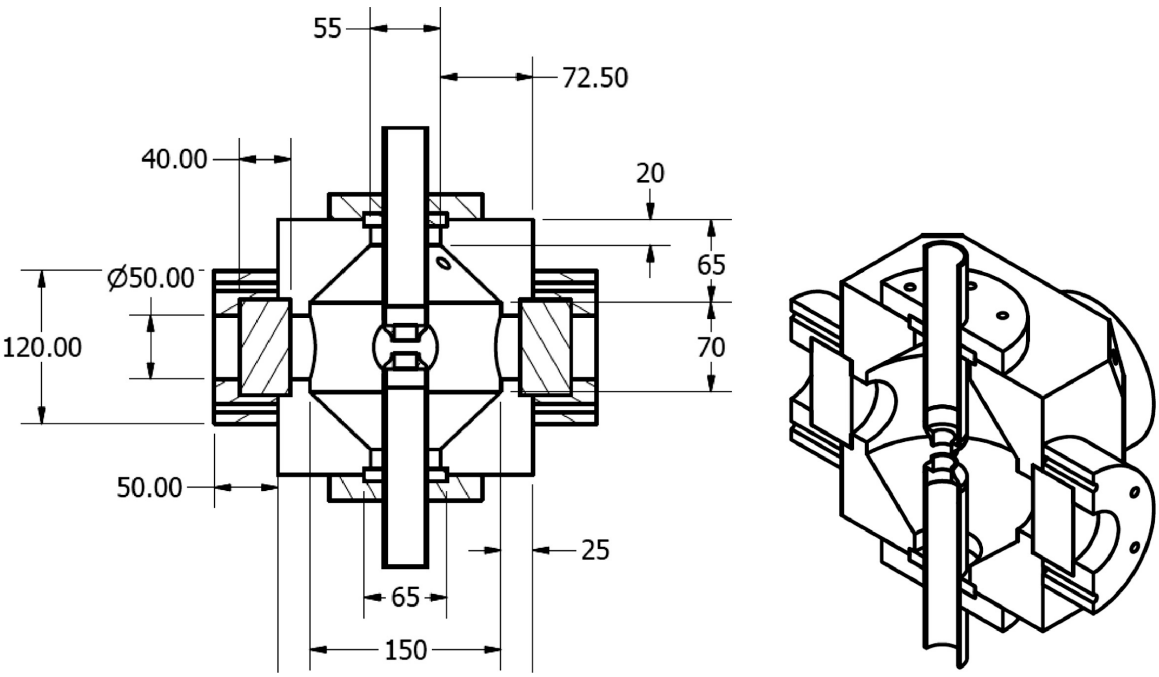

Figure 2.1: Schematic of the UVa counterflow burner with units in mm, from Sarnacki [1].

In experiments, the oxidizer, fuel and inert gases were metered and controlled by a series of Sierra model 100 mass flow controllers. The controllers have a factory calibrated accuracy of ±1% of full scale and repeatability of ±0.2% of full scale. All controllers were interfaced with using an existing LabView graphical user interface (GUI). The two impinging jets of oxidizer and fuel had the flux of their momentum matched according to the equation $\rho_{ox} \times v_{ox}^2 = \rho_f \times v_f^2$ where ρ_{ox} is the oxidizer stream density, v_{ox} the average oxidizer nozzle exit velocity, ρ_{fuel} the fuel stream density, and v_{fuel} the average fuel nozzle exit velocity. The average nozzle exit velocities were determined using the volumetric flow rate and nozzle cross sectional area. For the purposes of this paper, the axial velocity profile is assumed radially uniform across the nozzle exit. Additionally, the nozzles were machined with a contour designed to minimize the boundary layer and boundary layer instabilities at the nozzle exit plane [54] such that the flow does not diverge downstream of the tube exit and can be modeled as plug flow. The global strain rate is a function of the exit velocities and is defined as the ratio between the relative flow velocity of the fuel and the oxidizer stream and the nozzle separation distance L for an axially symmetric counterflow burner geometry. The calculation for global strain used in the following experiment is given by

$$a_g = 4v_{ox}/L \tag{2.1}$$

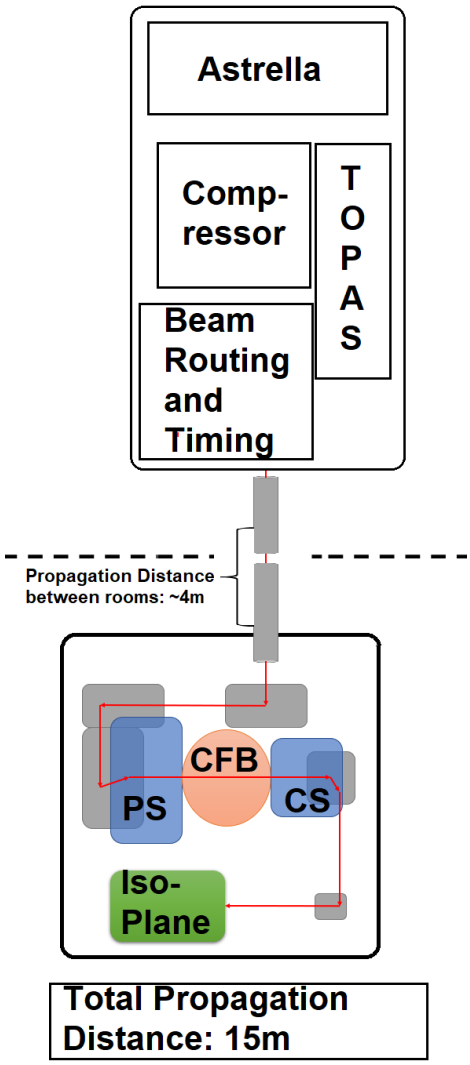

Figure 2.2: A schematic of the optical layout including the laser lab space and the burner lab space. Beam propagation is shown through the counterflow burner and into the 0.32m IsoPlane spectrometer. CFB-Counterflow Burner, PS-Pitch Stages, CS-Catch Stages.

For a specified global strain rate, the LabView interface automatically assigns all flow meter settings.

The chamber operating pressure was regulated using an existing back-pressure regulator (rated to 150 psig) controlled by a stepper motor. The chamber is equipped with a pressure relief valve and burst disk rated to 65psig and 110 psig to prevent over-pressurization. For the purpose of ignition at elevated pressures, the chamber that houses the counterflow burner's nozzles is backpressured using unheated air and N_2. Once the the correct pressure is reached, fueling and ignition are initiated. The fuel is diluted by 20% N_2 to help stabilize the flame closer to the center of the burner and extend the region over which CARS is sensitive. The LabView interface is then updated with the

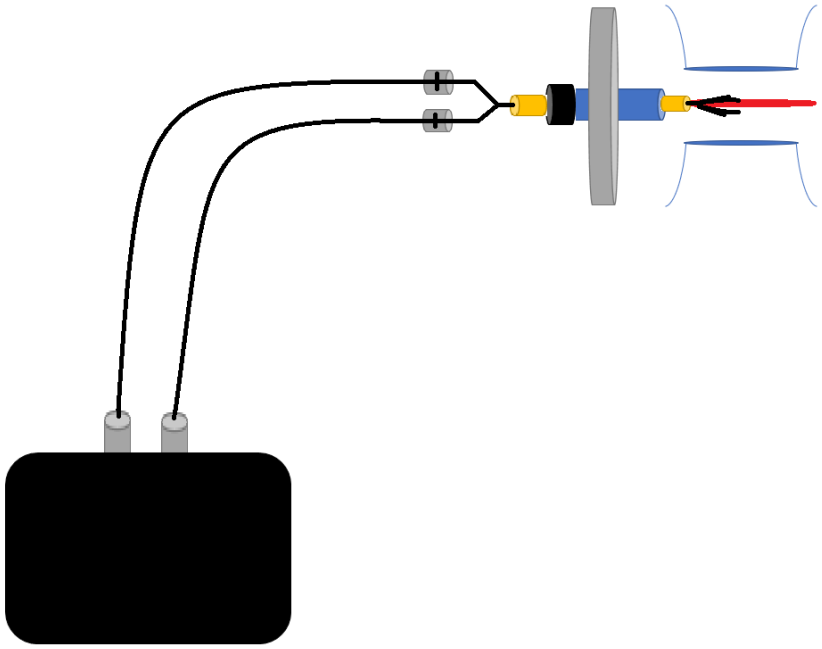

Figure 2.3: Modified ignitor to enhance ignition performance within the counterflow burner.

operation pressure and strain desired for the experiment, and the backpressure valve is adjusted until the chamber pressure matches the input.

2.1.1 Repeatable Ignition

Ignition of the counterflow burner at elevated pressures can be time consuming without a repeatable procedure. Originally, repeated manipulation of a high voltage electrode connected to a 10,000 V transformer was required to co-locate the spark and the axial location of optimal reactant diffusion. The electrodes are fed into a plunger sealed within an aluminum blank. This mechanism controls the depth of the electrode within the counterflow burner and assists with setting the correct height of the electrode. However, the insulative jacket around the electrode leads is stiff, and adjustment of the electrode's depth often torqued the wire, offsetting the position of the electrodes. If restricting and resetting the electrode's position was not done with careful attention, e.g. working with the electrode leads disconnected from the transformer, repeated handling of the electrode not only led to inconsistent ignition, but posed a safety hazard. Therefore, several key changes were made as shown in Fig. 2.3. One modification involved machining the electrodes down from the original diameter of $\sim$3 mm to a diameter of $\sim$1.1 mm such that they were no longer exceptionally large compared to

the distance between the nozzles. Another significant change was bisecting the insulated wire that connected the electrode to the transformer. This allowed for the wire leading to the electrode to be anchored using stationary posts such that routing to the transformer could no longer unintentionally shift the electrodes within the burner once placed. An additional benefit from the addition of the posts used to anchor the wires was the ability to consistently set the height at which the electrode was located relative to the nozzles. Placement of the electrode through the aluminum blank remained the same as it was deemed the most effective way to quickly push in or retract the electrode from the ignition point. The positioning of the electrode was informed through monitoring its location with respect to the nozzles using two cameras positioned at two perpendicular windows. This ensured the correct depth and height was used to guarantee the most repeatable ignition conditions.

2.2 Hencken Burner Adiabatic Flame Setup

In addition to the counterflow flame measurements, validation temperature measurements within a well-characterized, near adiabatic, H_2-air flame (Hencken burner) were conducted. These measurements were used to validate the fs/ps vibrational CARS temperatures by testing the system using a predictable, high-temperature gas. The honeycomb structure of the Hencken burner is a 50 mm by 50 mm plate with interspersed fuel and oxidizer jets for optimal mixing[30]. Surrounding the jets of fuel and air is a coflow of N_2 gas that serves to isolate the flame from ambient oxygen which could otherwise diffuse into the reaction. The burner has been the subject of detailed investigations using CARS to measure temperature, product and it provides a nearly uniform environment matching adiabatic flame temperatures [30]

CARS spectra were recorded at a height of 3.81 cm above the surface of the burner. This height was used to match the location within the combustion products where the adiabatic flame temperature is reached, as shown using a previous CARS experiment [30].

The combustion product temperature was varied by adjusting the fuel-air ratio for a constant air flow rate and constant N_2 coflow flow rate. For the complete combustion of hydrogen in air,

$$H_2 + a\,(O_2 + 3.76\ N_2) \rightarrow H_2O + (a - 1/2)O_2 + 3.76a\ N_2 \tag{2.2}$$

where $a = 1/2$ for stoichiometric conditions. The equivalence ratio, defined as the local fuel-air ratio divided by the stoichiometric fuel-air ratio, can be rewritten in terms of a as

$$\Phi = \frac{(F/A)}{(F/A)_{\text{stoich}}} = \frac{(1/4.76a)}{(1/4.76a_{\text{stoich}})} = \frac{a_{\text{stoich}}}{a} = \frac{1}{2a} \tag{2.3}$$

where F and A have units of molar flow rate and the fuel-air ratio is written as a function of ϕ.

$$\frac{F}{A} = \frac{1}{4.76a} = \frac{2\Phi}{4.76} = 0.420\Phi \tag{2.4}$$

Assuming standard temperature and pressure, molar and volumetric flow rates are equal. Therefore, given the equivalence ratio of interest and the flow rate for either air or fuel, the other can be subsequently calculated.

The flame temperature can be determined from the First Law of Thermodynamics

$$n_r \sum_i \chi_{i,r} h_{i,r} = n_p \sum_i \chi_{i,p} h_{i,p} + Q_{\text{out}} \tag{2.5}$$

where n_r and n_p are the total moles of reactants and products respectively (kmol), $\chi_{i,r}$ and $\chi_{i,p}$ are the mole fraction of reactant and products respectively, $h_{i,r}$ and $h_{i,p}$ are the molar enthalpies of reactant and products respectively (kJ/kmol), and Q_{out} is the heat transfer from the products (kJ) to the surroundings. For adiabatic conditions, $Q_{out} = 0$, the First Law can be written as $H_{r,tot}(T_r) = H_{p,tot}(T_p)$ and the product temperature can be calculated.

For the collection of validation spectra, the equivalence ratio was varied from 0.3 to 1.9 through controlling the flow rates of both oxidizer and fuel. The air flow rate was held constant using a 0 to 100 standard liter per minute (SLPM) mass flow controller (Alicat Scientific) with an accuracy of $\pm$(0.8% of the reading + 0.2% of full scale). For the constant flow rate of 60.6 SLPM used for air, the approximate error for read flow rate is 0.685 SLPM. To vary the equivalence ratio, the fuel flow rate was varied from $\sim$7 and 48 SLPM corresponding to ϕ 0.3-1.9. The mass flow rate uncertainty yields a maximum equivalence ratio uncertainty $\delta\phi = \pm 0.04$ and temperature uncertainty $\delta T = \pm 17$ K at $\phi = 1.0$. The adiabatic flame temperature for a $H_2 - air$ flame is expected to range from 1200 to 2400 K over the desired equivalence ratio range.

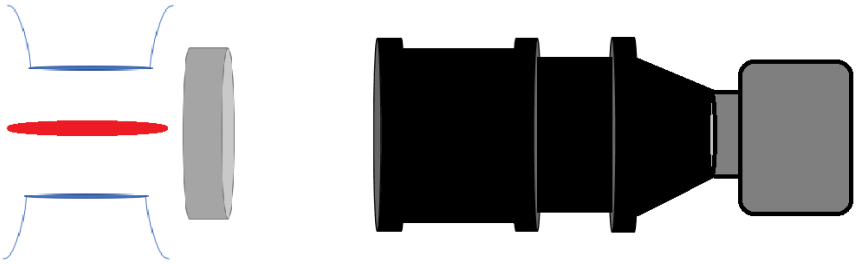

Figure 2.4: FLIR CMOS set outside of the counterflow burner to capture flame chemiluminescence images.

2.3 Flame Emission Imaging

Flame emission images were captured for each pressure and strain condition recorded for this experiment using a FLIR Chameleon 3 USB CMOS camera with a measured resolution of 8.46 $[\mu m/pix]$ from a total of 47 mm of tube extensions and an 85 mm focal length objective at an acquisition rate of 15.6 Hz and an exposure time of 58.8 ms. The FLIR camera was set at a fixed distance where the entirety of the flame's domain and both fuel and oxidizer nozzles could be imaged. An experimental schematic is shown in Fig. 2.4.

Flame emission images served to visualize approximate flame location during the experiment relative to the fuel nozzle, analyze flame shape variation, and observe the amount the flame deviates from its mean position over time.

2.4 CARS Layout

A dual-pump fs/ps CARS system similar to what have been reported by Geipel [5] and Dedic et al. [55] was utilized. An ultrafast Ti:sapphire laser (Astrella, Coherent) with a 7 mJ, 60 fs output pulse centered at 798 nm is used to pump an optical parametric amplifier with harmonic generation (Light Conversion, TOPAS-Prime) to produce frequency-doubled signal at 676 nm. The CARS 28 μJ pump ($\omega_1 = 14793$ cm^{-1} with $\Delta\omega \sim 180$ cm^{-1}) and 32 μJ Stokes ($\omega_2 = 12531$ cm^{-1} with $\Delta\omega \sim 150$ cm^{-1}) preparation pulses were temporally and spatially overlapped to excite ro-vibrational transitions in the N_2 molecule near 2330 cm^{-1}, as labeled as ω_{vib} in Fig. 2.5a. A pulse-shaped narrowband probe beam at 798 nm interacts with the vibrational beating frequency through the BOXCARS phase-matching configuration and generates a CARS beam which carries the spectral signature of the N_2 ro-vibrational energy distribution. The probe pulse can be temporally delayed (τ in Fig. 2.5b) via a high-resolution motorized delay stage (ILS150PP, Newport). This allows for the suppression of

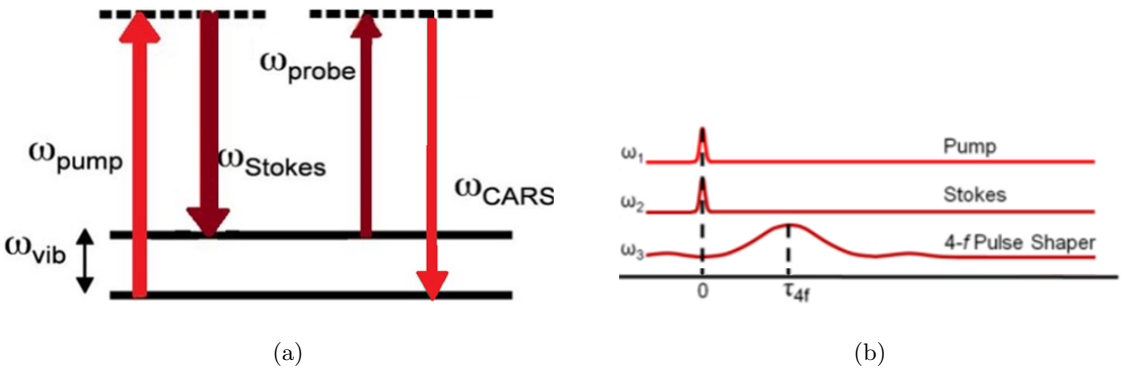

(a) (b)

Figure 2.5: (a) Energy diagram for hybrid fs/ps CARS beams, and (b) timing diagram illustrating temporal lineshapes of pump and Stokes compared to probe's generated with 4-f pulse shaper delayed to some time τ_{4f}.

non-resonant background as will be discussed in Chapter 3. The CARS spectra were recorded with a 0.32-m spectrometer (IsoPlane-320, Princeton Instruments) utilizing a 1200 line/mm grating and an electron-multiplying, charge-coupled device (EMCCD, ProEM, Princeton Instruments), resulting in an effective detector resolution of ∼0.034 nm.

The probe pulse shape employed to conduct thermometry within the counterflow burner was created using a folded 4-f pulse shaper. A 4-f pulse shaper is commonly used in fs/ps CARS experiments to generate an adjustable width ps probe pulse. An adjustable width probe pulse was desirable as the non-resonant response was relatively more apparent at higher temperatures. The ability to suppress the nonresonant contribution while still maintaining temperature sensitivity was an important consideration for probe-pulse optimization. As shown in Fig. 2.6, a broadband fundamental pulse at 798 nm, which exhibits a near Gaussian profile, was dispersed in space via an estimated 1200 l/mm grating and then focused onto a mirror set at the Fourier plane by a 250mm cylindrical lens. An adjustable spectrometer slit placed at the Fourier plane acts as a flat-top spectral filter in the frequency domain, allowing the linewidth to be arbitrarily selected. As the pulse was reflected back to the grating, it was recombined into a beam and used as the CARS probe pulse. In the current study, slit width and probe delay were adjusted while observing spectral response in a flame until the non-resonant signal was optimally suppressed. A scan of the probe temporal response in a non-resonant gas, Ar, revealed an approximately sinc^2 probe shape with a FWHM spectral linewidth of 6.5 cm^{-1} was utilized. The overall throughput of the 4-f pulse shaper at 798 nm was ∼2% for the chosen slit width.

An overview of the optical table housing the Astrella and the fs/ps CARS system is shown in Fig. 2.2. For further information concerning the layout of the CARS experiment refer to Geipel

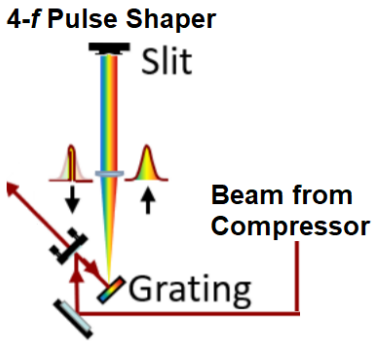

Figure 2.6: Folded 4-f pulse shaper used in shaping the probe temporal profile.

[5]. In the laser laboratory room, each beam was routed through necessary pulse shaping, frequency conversion, and optical delay lines before being propagated into the burner room. The beams were directed from the Astrella room through a port to a three axis translation stage system located in an adjacent room. Each of the three beams were routed through separate periscopes on the stage system to reach the correct height for performing CARS within the counterflow burner as is shown in Fig. 2.8. The optics on the final breadboard allow for fine adjustment of the beams to their individual lenses through the counterflow burner. Thorlabs linear motion controllers were setup on the opposite side of the burner to catch the CARS signal, which was spatially separated from the outgoing beams, collimated and directed to the spectrometer.

To ensure proper spatial and temporal overlap of the three beams, the BOXCARS phase matching configuration discussed earlier was utilized. A pair of adjustable mirrors for each beam was used to center the beams on two spatial masks placed before and after the counterflow burner located two focal lengths (f=300 mm) away from one another. Next, a beam splitter was used to direct 4% of the beams' intensities through multiple neutral density filters to a FLIR blackfly camera (measured resolution of 3.45 $\mu m/pix$) to observe the spatial location of each beam at the probe volume. The camera and filters were set on micrometer-driven translation stage to locate and adjust the position of each individual beam waist and to control the amount of astigmatism at the location of beam overlap. Because each focusing lens was manipulated individually, each beam can be spatially overlapped at a designated distance away from their relative foci. The importance of this is shown by Geipel [5], as choosing crossing locations for spatial overlap controls the length of the probe volume and influences the amount of beam energy that can be used before inducing breakdown within the CARS probe volume. For this experiment, the beams were crossed 2.55 mm before the foci of the Stokes and pump beams to match the approximate diameter of probe, set at its focus. Third, temporal overlap

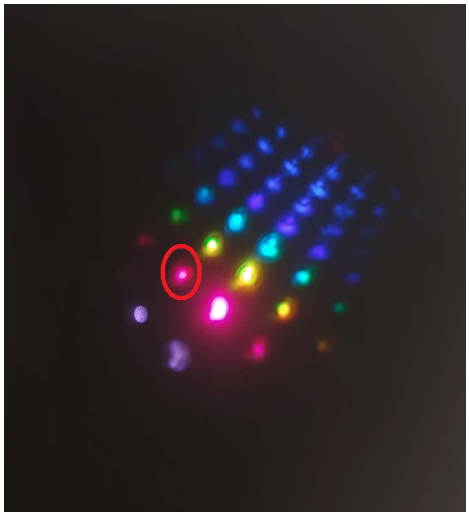

Figure 2.7: CARS signal generation in a thin piece of glass (red circle) used to optimize spatial and temporal overlap.

between the three beams was monitored using a photodiode (2 ns rise time) aimed at the probe volume and oscilloscope (Textronix, 500 MHz) while adjusting each optical delay line. This method for obtaining temporal overlap was used to accurately locate each beam in time within 30 ps of one another. Finally, a ∼0.13mm thick glass coverslip was placed at the CARS measurement volume and spatial and temporal overlap were adjusted to achieve maximum CARS signal generation in glass. A photograph of the generated signal in glass is shown in Fig. 2.7 A second three-axis stage system was located after the counterflow burner containing collection optics. A spatial mask was used to block the input beams and allow only the CARS signal to propagate through the stage system. A f=300 mm lens was used to collimate the generated CARS signal and mirrors were used to direct the signal from the stage system to the spectrometer. Finally, a f=60 mm lens was used to couple light into the spectrometer slit. The spectrometer was placed ∼1.2 m away from the burner to limit the amount of luminous noise generated by the counterflow flame. A spatial filter comprised of two plano-convex lenses (focal lengths of 150 mm and 200 mm) and a 100 μm pinhole was utilized before the focusing lens as a spatial filter to assist with minimizing pump laser scatter background flame emission.

Initial alignment of the CARS collection optics was executed using signal generation in glass. However, because the glass imposes a physical restriction on the CARS measurement location compared to signal generated in a gas, final alignment was performed without the glass by visualizing light scatter from a laser-induced plasma at the probe volume created by increasing the Stokes beam

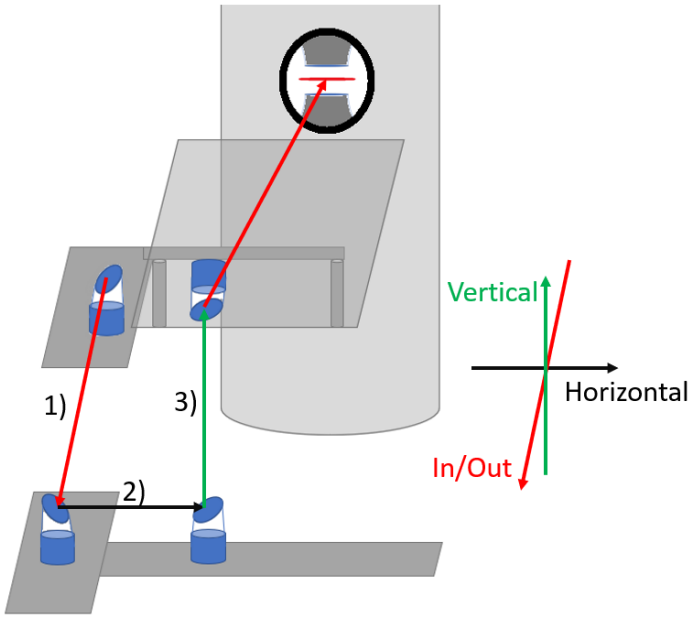

Figure 2.8: Beam path leading to the top plate on the pitch stage with mirror positions corresponding to each axis of translation: 1) Horizontal in/out translation. 2) Horizontal across burner face. 3) Vertical translation.

energy to 897 μJ. This light was observed to follow the same route as the actual fs/ps CARS signal, serving as a useful alignment tool.

2.5 Mobile Stage

To route the beams through the counterflow burner, a three-axis mobile stage system was developed. Proper alignment of this system is necessary to allow for the precise positioning of the probe volume within the flame. By aligning each of the turning mirrors with the corresponding axis of translation, the mobile stage system could be accurately aligned to reduce beam misalignment during translation. The alignment procedure will be further discussed in the following chapter. Translation horizontally and vertically across the burner face was accomplished using Kinger UT100 stepper-motor linear ($0.1\mu m$ resolution) whereas the translation of the probe volume into and out of the burner was accomplished using a manual stage to move the optics a set distance away from the burner. On the opposite side of the burner was a second translation stage system to collimate and direct the CARS signal to the 0.32m spectrometer. This system used two Thorlabs LNR502 linear stepper motor stages (0.02μm resolution).

Chapter 3

Fs/ps CARS system stability

3.1 Stability Analysis of Beam Drift

Prior to conducting fs/ps CARS measurements within the counterflow burner, several issues impacting CARS signal stability required addressing. After initial alignment of the fs/ps CARS system within the counterflow burner, the CARS signal intensity immediately diminished over the span of 5 minutes. Spatial beam drift was identified as the primary issue and required a thorough investigation to enable usable fs/ps CARS measurements. To determine the sources of the spatial drift, a beam profiling camera (FLIR Blackfly CMOS, measured resolution of 15.2 $\mu m/pix$) was utilized to track the position of each beam's centroid over time. Example beam profiling images are shown in Fig. 3.1. Panel a) shows the raw image recorded using the beam profiling camera, while 3.1b) shows the detected centroid with corresponding coordinate values. These values are exported to MATLAB for live processing to measure changing beam positions with time. Beam drift was first recorded in the lab housing the laser and delay lines (hereafter referred to as the "Laser Lab") to narrow down sources of instability between the two laboratory spaces. Shown in Fig. 3.3 are the Stokes and probe beam positions recorded every 15 seconds for one hour. As the spatial location of the Stokes beam was nearly constant, it was used as the reference beam to compare to probe beam displacement. The displacement of the pump beam was observed to be on the same order as Stokes and is not shown. Panels a) and b) show beam positions measured within the Laser Lab before and after system upgrades, respectively. As seen in Fig. 3.3a), the probe beam initially experienced significant beam drift. It not only drifted spatially over time, but the probe beam drift was not repeatable: beam locations recorded at the beginning and end of each day revealed that the

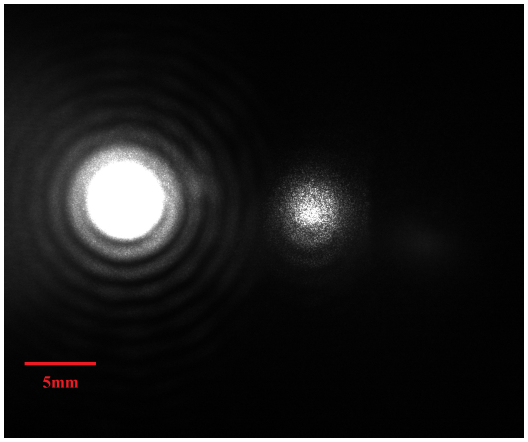

(a)

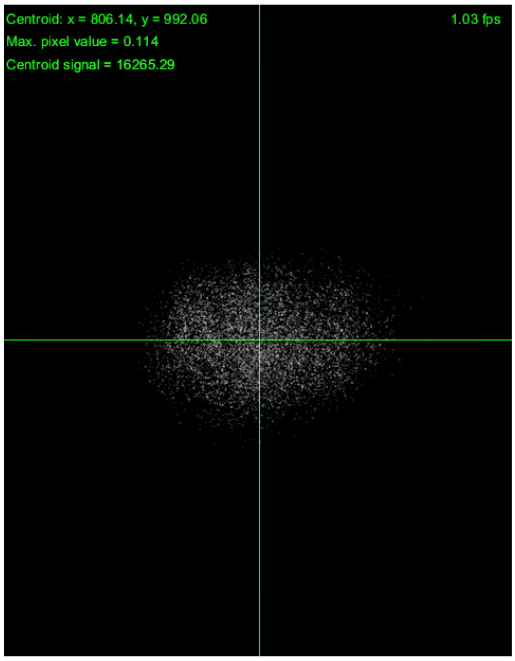

(b)

Figure 3.1: (a) Raw image recorded by the camera and used by the centroid finding routine. (b) Processed image with centroid coordinates labeled.

beam never returned to its initial position nor ever ended in a similar final position between days. Therefore, it was concluded that the drift was likely due to an unstable optic or set of optics rather than a repeatable drift resulting from the laser warming up or a change in the room temperature. To identify the unstable optics, multiple pick off mirrors were placed at various locations along the probe path as shown in Fig. 3.2. The positions selected were 1) after the external compressor to the Astrella, 2) after the 4-f pulse shaper, 3) between the 4-f pulse shaper and the probe delay stage, and

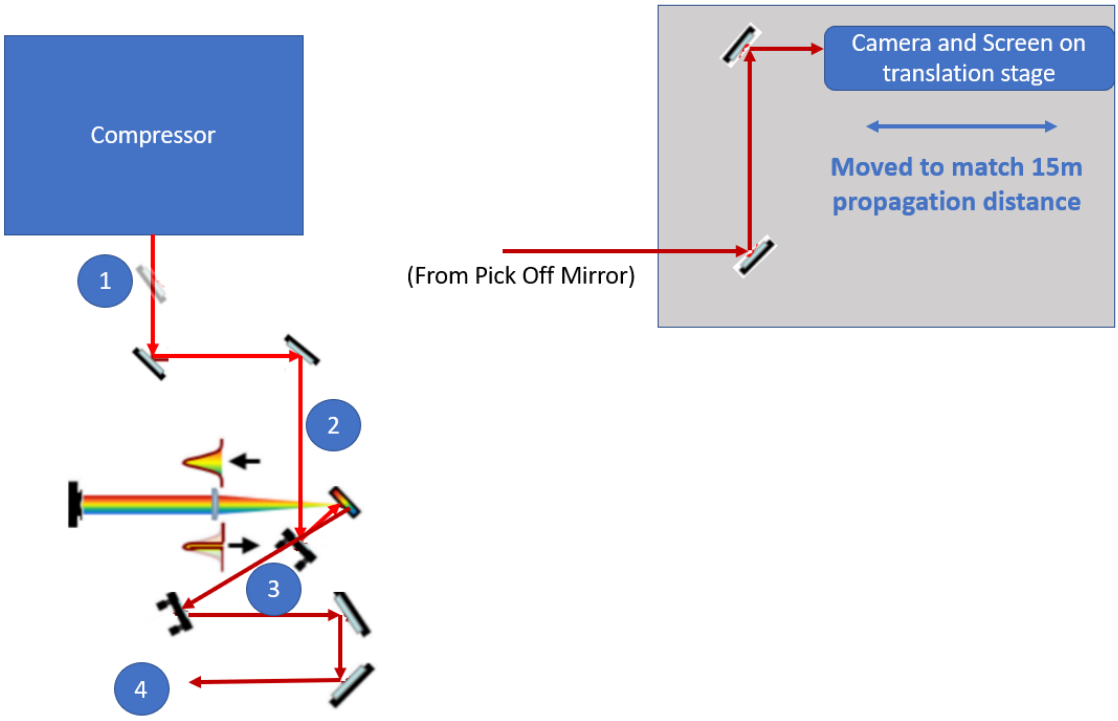

Figure 3.2: Pick off mirror locations in probe beam path to investigate beam instability.

4) after the probe delay stage. To match the total propagation distance to the counterflow burner, the path length from a pick off mirror to the beam profiling camera was set to 15 m within the Laser Lab. The constant propagation distance ensured that the magnitude of spatial displacement observed was not a result of differing path lengths. This procedure revealed that the observed spatial drift primarily originated from the 4-f pulse shaper. To address the issue, mounts and mirrors were replaced individually and the impact on spatial drift was monitored after each adjustment. The grating mount was identified as the primary culprit, and, following its replacement, the displacement of the probe beam was within an acceptable margin. Figure 3.3b demonstrates the significant improvement observed after replacing the grating mount.

After ensuring the stability of each beam within the Laser Lab, the laser was propagated to the next room housing the counterflow burner (hereafter referred to as the "Combustion Lab") where the process for monitoring stability was repeated. The beams were imaged on a screen mounted before the three axis translation stage using the same beam profiling camera, as shown in Fig. 3.4. As can be seen in Fig 3.5b), another source of instability was identified.

Because the spatial drift was observed prior to the first turning mirror within the Combustion Lab, the source of instability could not be an optical component. Instead, the beam tube used

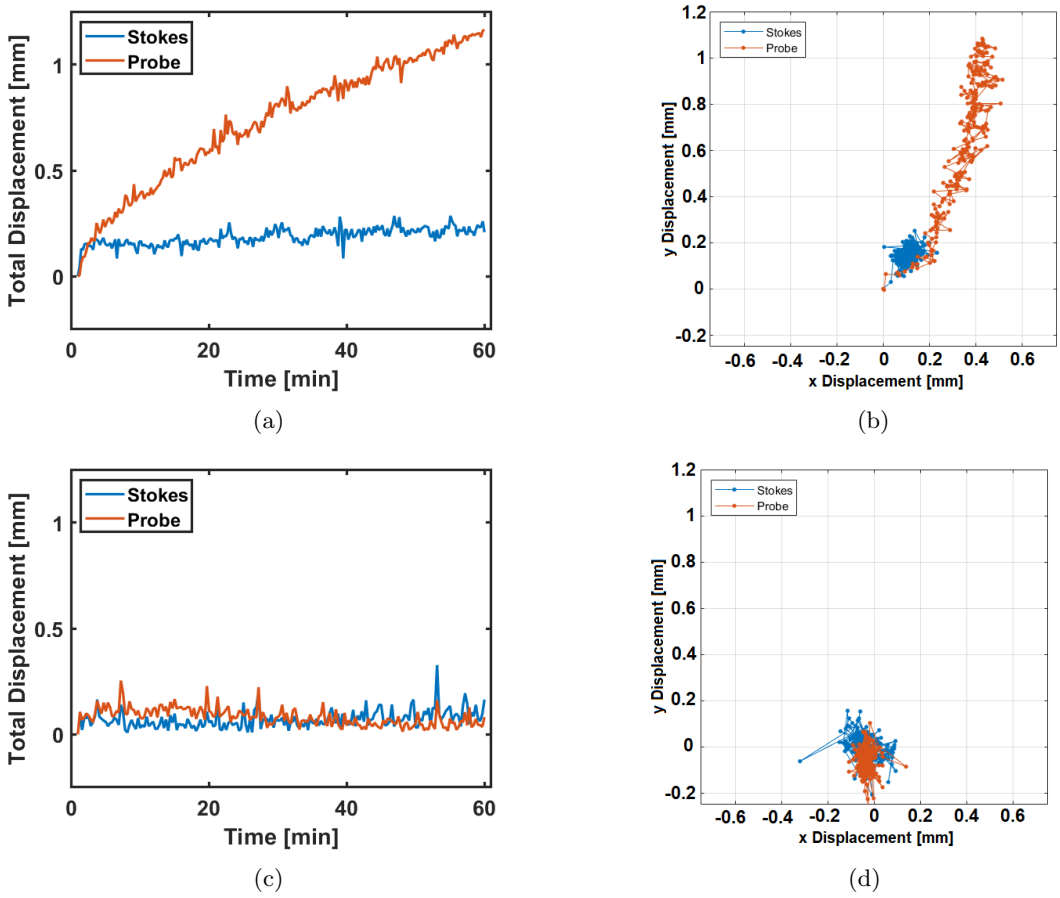

Figure 3.3: (a) Pump and Stokes spatial displacement as a function of time recorded in the Laser Lab space. (b) Two-dimensional spatial displacement shown relative to the initial position. (c) Total beam displacement over time in the after replacement of unstable optics. (d) Two-dimensional spatial displacement shown relative to the initial position.

to enclose the beams as they propagated between rooms as a safety precaution was identified as the primary issue. The reasoning for this issue was traced to the laboratory building itself. Each laboratory space uses its own heating, ventilation, and air conditioning (HVAC) system and are controlled separately. During the month of February, the temperature of the room housing the fs laser and majority of the fs/ps CARS system remained fairly constant throughout the day, only fluctuating by 1°C. In contrast, the Combustion Lab experienced a cyclic change in temperature of 4°C every 15 minutes as the HVAC system turned on and off. Temperature gradients between the two rooms caused air to be forced through the beam tube. This led to the conclusion that density gradients within the 3 m long tube were resulting in noticeable beam drift. From cutting holes to minimize thermal gradients within the tube to increasing the diameter of the tube, several attempts were made to mitigate the source of instability. The final, successful action taken was to bisect

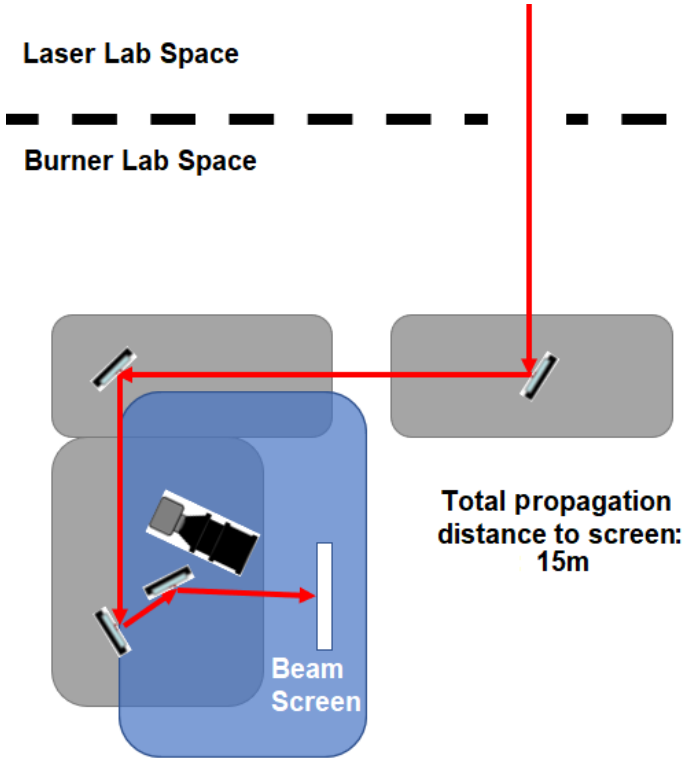

Figure 3.4: Propagation followed along the beam path from the Laser Lab space to the burner lab space to investigate beam instability atop the three axis stage system.

the tube at the port connecting the two laboratory spaces, preventing the tunneling of air between the rooms. Fig. 3.5c,d) demonstrates the resultant beam positions measured over time, showing a distinct improvement from Fig. 3.5a,b). The final change made to ensure system stability was to enclose the top of the optical table housing the counterflow burner with acrylic to shield the long beam paths from any additional temperature gradients or air currents caused by the HVAC system. With this concluded, alignment of the three beams through the mobile stage system could begin.

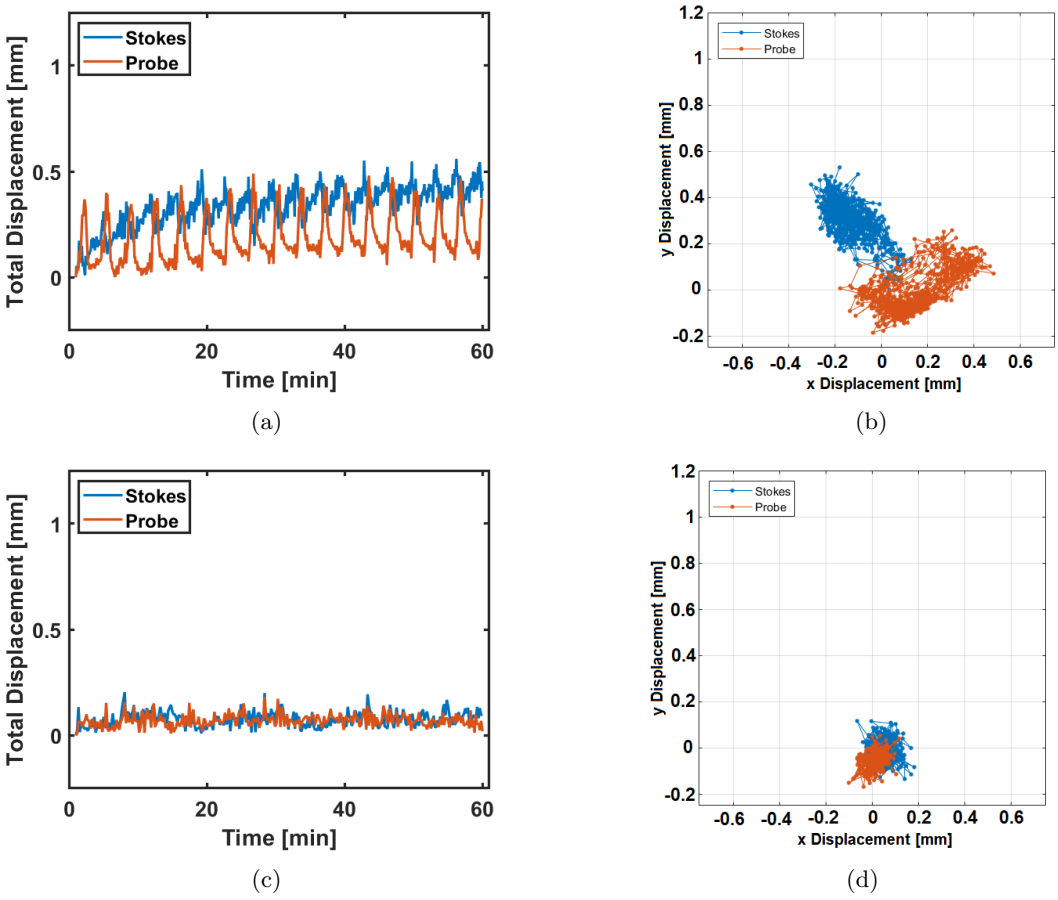

Figure 3.5: (a) Beam displacement as a function of time recorded in the room containing the counterflow burner. (b) Two-dimensional spatial displacement shown relative to the initial position. (c) Total beam displacement over time in the room containing the counterflow burner after bisecting the beam tube. (d) Two-dimensional spatial displacement shown relative to the initial position.

3.2 Three Axis Stage Controller Stability

Next, alignment of the beams propagating through the three axis stage system (hereafter referred to as the pitch stage) will be discussed. After alignment efforts to ensure signal stability over time, loss of CARS signal intensity during motorized translation of the stage system was observed. After ensuring that the routing of the CARS signal to the specrometer was not the cause, spatial misalignment of the crossing beams was suspected. The normalized signal intensity measured during a scan across the two motorized axes is shown in Fig 3.6. For both axes of translation, the signal failed to remain stable. The previously used beam profiling camera was used to image light scatter from a card placed immediately before each focusing lens on the pitch stage. The same processing routine using centroid detection and location tracking, was used to identify total spatial drift for a given axis as each translation stage was moved over a range of 50 mm. As suspected, the spatial location of each beam deviated from its initial point of overlap.

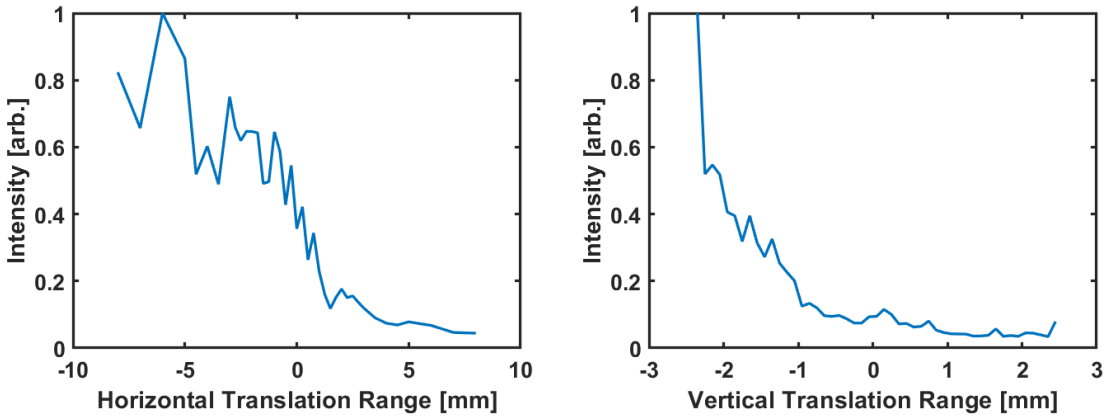

(a) (b)

Figure 3.6: (a) CARS signal intensity variation during a horizontal scan and (b) CARS signal variation during a vertical scan prior to alignment.

A more robust alignment procedure was required to ensure that the spatial location did not significantly deviate during the translation of the stages. The mirrors at each position in Fig. 2.8 were used to correspond to the alignment of a particular axis of translation. The alignment procedure chosen dictates that each beam be aligned in order from the furthermost mirror from the burner to the nearest. Adjustment of the furthermost mirror corresponds to the alignment for the horizontal in/out motion, the mirror following it aligns the horizontal translation across the burner face, and the bottom periscope mirror adjusts vertical alignment. An example of the alignment procedure for the horizontal in/out axis is as follows: The beam's centroid coordinates are found for

one extreme of the translatable distance, the stage is moved to the other extreme and the centroid's coordinates are recorded, the coordinates from the two locations are compared and the mirror is adjusted to compensate for spatial displacements that exceed 75 μm. The previous steps are then repeated until spatial displacement is within the 75 μm boundary which corresponds to the variance in spatial location for a stationary beam. This procedure is then repeated for each of the following axes, and then the other two beams. It is important to note that the beam path shown in Fig. 2.8 only corresponds to a single beam, each of the beams have their own set of mirrors for individual alignment.

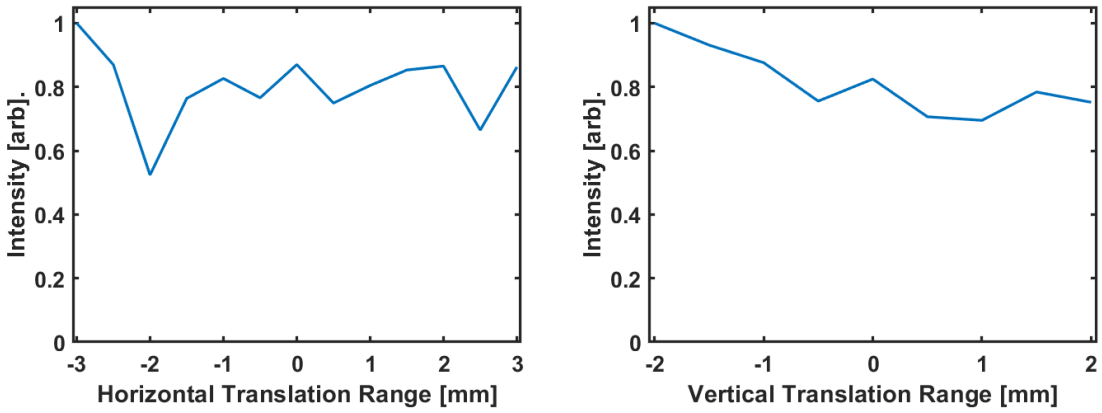

(a) (b)

Figure 3.7: (a) CARS signal intensity variation during a horizontal scan and (b) CARS signal variation during a vertical scan after alignment to minimize spatial drift.

By iteratively minimizing the spatial drift each beam experienced as the pitch stage was translated over a course of 50mm for each axis, the CARS signal was able to be properly maintained over the domain of interest as can be seen in Fig. 3.7. It was noted that there was a slight drop in CARS signal at the -2mm horizontal position which was attributed to mechanical backlash as the direction of horizontal translation was changed.

Chapter 4

Temperature Measurements of Counterflow Flames

4.1 Operation

4.1.1 Hencken Burner

After improving the stability of the fs/ps CARS system, measurements within a combustion environment could begin. To determine best fit temperatures, a library of theoretical spectra is needed to compare against those taken experimentally [4]. The spectral library must be populated with experimental parameters including bandwidth, chirp, time delay, and peak wavelength of each beam, and the detection instrument function before simulating spectra to compare with experiments. Before analyzing CARS data collected within the counterflow flame, a well-characterized, near-adiabatic H_2/air flame was used to test to validity of the CARS system and optimize spectral parameters used to simulate theoretical spectra. With spectral parameters informed in this manner, a differential evolutionary algorithm is then used to minimize the normalized residuals between theoretical spectra and experimental spectra from the near-adiabatic flame [4]. This routine outputs the parameters necessary to determine the spectral response of the simulated spectra to increasing temperature. With this, the spectral library is populated with simulated spectra that bear the same spectral parameters and temperature response as those collected experimentally.

A Hencken burner was chosen for preliminary measurements because its design eliminates heat transfer to the burner surface, allowing the combustion products to reach the adiabatic flame tem-

perature and making it an ideal system for collecting validation data [30]. Fs/ps CARS targeting N_2 rovibrational transitions is sensitive to temperatures above $\approx$ 1100K. Therefore, an equivalence ratio range of $\phi = 0.3$ to 1.5 was selected for the H_2/air mixture as it corresponds to an adiabatic temperature range of 1187 K to 2396 K. A constant flow rate of air and N_2 was selected, and the fuel flow rate was modified to change the equivalence ratio following Eq. 2.4 from Chapter 2. Experimental conditions employed are summarized in Table 4.1.

Table 4.1: Operating conditions used with the Hencken burner.

Equivalence Ratio ϕ	Fuel Flow Rate [SLPM]	Oxidizer Flow Rate [SLPM]	N_2 Shroud Flow Rate [SLPM]
0.3	7.64	60.6	85
0.4	10.18	60.6	85
0.5	12.73	60.6	85
0.6	15.28	60.6	85
0.7	17.82	60.6	85
0.8	20.37	60.6	85
0.9	22.92	60.6	85
1.0	25.46	60.6	85
1.1	28.01	60.6	85
1.2	30.55	60.6	85
1.3	33.10	60.6	85
1.4	35.65	60.6	85
1.5	38.19	60.6	85

4.1.2 Counterflow Burner

The counterflow burner's general operation was detailed in Chapter 2, and the operational parameters used for data collection are outlined here. As a reminder, the chamber pressure and desired global strain rate were input into a LabView interface, and the necessary gas velocities and flowrates were calculated and used as system set points. The selection of near extinction global strain rates was informed by Cantera using the GRI 3.0 mechanism [56] to simulate an axisymmetric flow for diluted CH_4/air diffusion flame. Cantera was used to calculate these simulations given inputs of initial species mole fractions of the fuel and oxidizer streams, pressure, domain conditions (nozzle distance), and sample conditions near extinction is included in Table 4.2. The strain rate at which extinction occurred as well as temperature profiles at those conditions were output.

The following pressures and strain rates were investigated: 2.5 atm at a low global strain rate of 450 [1/s], 2.5 atm near its extinction global strain rate of 900 [1/s], 4 atm at a low global strain rate of 500 [1/s], 4 atm at a near-extinction global strain rate of 1000 [1/s]. The lower pressure of 2.5

atm was the lowest pressure at which the flame stabilized in a location that allowed the entire flame to be characterized with CARS. The higher pressure of 4atm was chosen for being the most elevated pressure that could be characterized near extinction as beam steering effects for the current beam configuration near the stagnation plane greatly disturb the CARS interrogation volume leading to increasing sources of error. The corresponding experimental parameters used for the current study are summarized in Table 4.3. Included are the mass flow rates for the fuel (CH_4), oxidizer (air), fuel diluent (N_2), and shroud gas (N_2) corresponding to the desired global strain rates and global pressures investigated.

In addition to the CARS thermometry data collected within the counterflow burner, CARS spectra in an Argon gas environment were recorded to characterize the shape of the experimental probe pulse as generated using a 4f-pulse shaper. This data was also used to determine the probe delay relative to initial Raman excitation for the experimental measurements. Additional discussion regarding the influence of the probe pulse shape is included in the next section.

Table 4.2: Example of Cantera inputs for calculating near extinction global strain rates.

Pressure [atm]	Mechanism	Initial Global Strain [1/s]	Fuel Mole Fraction	Oxidizer Mole Fraction	Nozzle Distance [mm]
2.5	GRI 3.0 [56]	450	0.8 CH_4, 0.2 N_2	0.79 N_2, 0.21 O_2	5.45

Table 4.3: Table of operating conditions within the counterflow burner.

Pressure [atm]	Global Strain [1/s]	Fuel Side Flow Rate [SLPM]	Oxidizer Side Flow Rate [SLPM]	N_2 Shroud Flow Rate [SLPM]
2.5	450	3.22	3.44	11.25
2.5	900	6.34	6.63	21.89
4	500	5.67	5.84	22.31
4	1000	11.17	11.27	43.33

4.2 Numerical Modeling

The nonlinear, third-order polarization field is generated when a medium and the three electric fields from the pump, probe, and Stokes beams interact. This polarization field is constituted by a resonant and non-resonant response.

The resonant portion of the third-order polarization is given in Eq. 4.1. The $\times$ symbol is the convolution operator and $E_n e^{i\omega_n t_n}$ are the incoming electric fields with field strengths E_n, frequencies ω_n, and coherence times t_n.

$$\begin{aligned} P^{(3)}_{\mathrm{CARS}}(t,\tau_{12},\tau_{23}) = \left(\frac{i}{\hbar}\right)^3 \int_0^\infty dt_3 \int_0^\infty dt_2 \int_0^\infty dt_1 \, [R_4(t_3,t_2,t_1) \\ \times E_3(t-t_3)\, E_2^*(t+\tau_{23}-t_3-t_2) \\ \times E_1(t+\tau_{23}+\tau_{12}-t_3-t_2-t_1) \\ \times e^{i(\omega_1-\omega_2+\omega_3)t_3} e^{i(\omega_1-\omega_2)t_2} e^{i\omega_1 t_1}\Big] \end{aligned} \tag{4.1}$$

The subscripts 1, 2, 3 and 4 correspond to pump, Stokes, probe and CARS respectively. Each electric field, $E_n e^{i\omega_n t_n}$, is assumed to be centered about $t = 0$; therefore, the time delays τ_{23} and τ_{12} correspond to the delays between the Stokes and probe pulses and the pump and Stokes pulses respectively. R_4 is the molecular response function for the CARS process, and is often assumed instantaneous over the t_1 and t_2 timescales. However, CARS signal is not solely comprised of the resonant polarization, but is actually proportional to the square of a portion of the third-order polarization terms arising from non-resonant and resonant wavemixing as shown in Eq. 4.2 [48, 19, 57, 58, 5].

$$I_{\mathrm{CARS}}(\omega,\tau_{12},\tau_{23}) \propto \left| P^{(3)}_{NR}(\omega,\tau_{12},\tau_{23}) + P^{(3)}_{\mathrm{CARS}}(\omega,\tau_{12},\tau_{23}) \right|^2 \tag{4.2}$$

To match experimental work, the delay of the two fs pulses, the pump and Stokes beams, τ_{12}, was set to zero. The time delay of the ps probe pulse with respect to the other two is represented . Non-resonant polarization contributes greatly to the background when all three beams are temporally overlapped, but dephases quickly if the ps pulse is offset from the two fs pulses. As a result, the non-resonant contribution may be neglected when the probe delay is significantly greater than the delays of the other two pulses, $\tau_{23} > \tau_{12}, [\tau_{12} = 0]$ [48, 47, 57, 58, 5, 4]. Therefore, the non-resonant term is typically neglected for fs/ps CARS experiments using a time-delayed probe pulse.

4.2.1 4f Pulse Shape Model

Because suppressing non-resonant background by delaying probe greatly simplifies spectral modeling, it was critical to accurately represent the ps probe shape within the model. To ensure the pulses have the minimum possible duration for a given spectral bandwidth, the spectral lineshape is related to the time-domain lineshape by way of the Fourier Transform. For the 4-f pulse shaper with a

square slit, the Fourier Transform is a sinc^2 function that exhibits several side lobes of decreasing intensity in time. This time profile is shown in Fig. 4.1a, which plots two modeled probe shapes for a sinc^2 and Gaussian function given the same FWHM spectral linewidth. Using these simulated probe shapes, the impact on the simulated spectra is shown in Fig. 4.1b. The presence of side lobes of the sinc^2 pulse shape demonstrate that a model incorporating only an idealized Gaussian probe shape would not accurately simulate the CARS response observed experimentally.

As non-resonant contributions were more evident at higher temperatures, slit width and probe delay were adjusted while observing the spectral response in a flame until the non-resonant signal was suppressed. A cross-correlation of the probe pulse with the impulsive Raman excitation was then recorded using nonresonant CARS signal in Argon gas by scanning the probe delay stage in time at a speed of 0.1 ps/s. A 0 ps time delay corresponds to the maximum non-resonant background intensity as all three beams are overlapped in time. The delay stage was scanned from -20 ps to +20 ps, during which 4200 frames were acquired at a rate of 10.5 fps. Integrating the non-resonant signal for each frame was used to quantify the experimental probe shape. In Fig. 4.2, the experimental probe shape shown in Fig. 4.2a, and its comparison to best-fit probe shapes for both a Gaussian and sinc^2 in Fig. 4.2b. In Fig. 4.2b, it can be seen that neither the Gaussian or sinc^2 fits to the probe-pulse well. The experimental probe shape resembles a composite of the two functions. The non-ideal shape is likely due to a misalignment of the 4-f pulse shaper resulting in a deviation from the transform limit, for example, a tilted slit at the Fourier plane. This slight disagreement may also be due to the frequency domain not exhibiting a flat-top spectral profile at the center of the slit. Future improvements of the system will seek to more thoroughly characterize the probe response to different slit widths. However, the probe delay where non-resonant contributions will be minimized can still be determined. The minima of the first side lobe for the experimental probe pulse corresponds to a probe delay of $\sim$5.0 ps. At this delay, the non-resonant signal level was minimized while the resonant signal intensity was maximized.

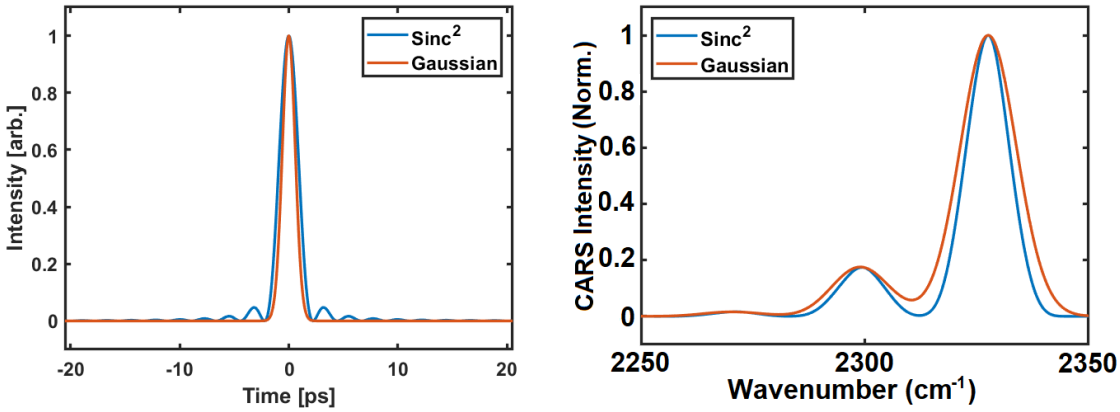

(a) (b)

Figure 4.1: For the same FWHM a) two modeled probe shapes in time, b) simulated spectra for each probe shape at a delay of $\tau = 2.225$ps, corresponding to the first minima in the sinc^2 probe shape shown in a).

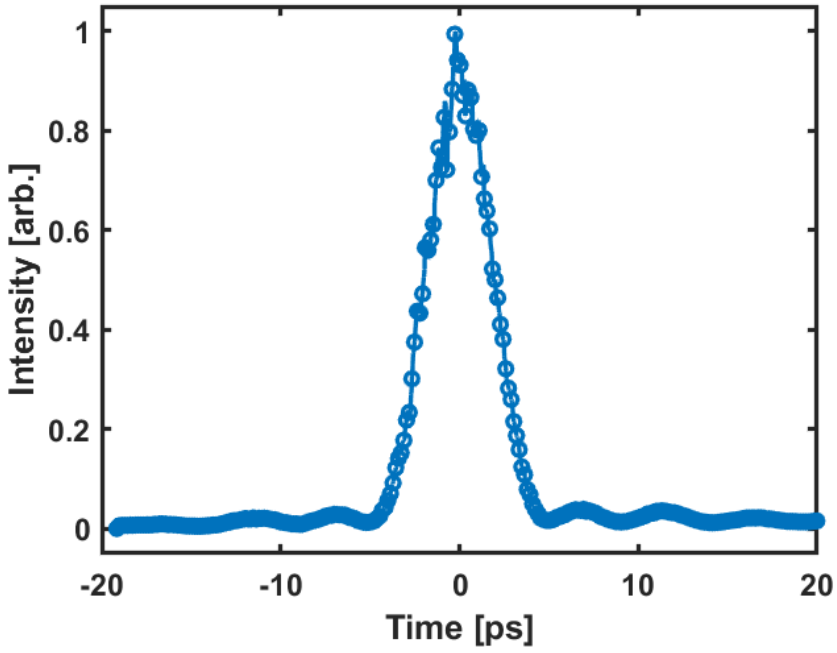

(a)

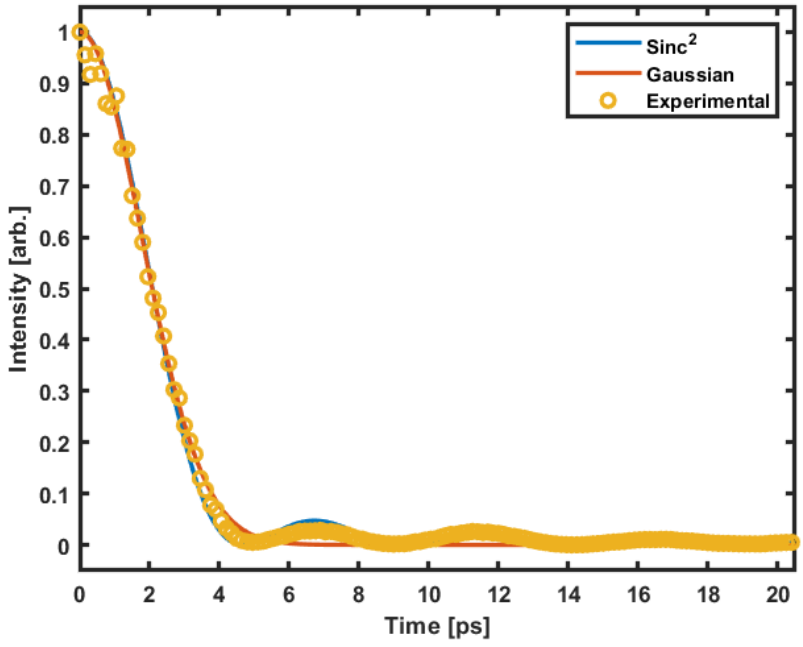

(b)

Figure 4.2: a) Experimentally measured probe shape in Ar. b) Experimental probe shape after time zero compared to Gaussian and sinc^2 probe shapes.

4.2.2 Spectral Fitting Routine

To determine gas temperature, experimentally collected fs/ps CARS spectra were compared to spectral simulations. A differential evolutionary algorithm, as informed by Mallipeddi et al [59] and previously implemented by Dedic [4], was then supplied a library of simulated spectra at temperatures ranging from 900 K to 2800 K and experimental spectra to determine best fit temperatures. The data processing routine used for this work is outlined below.

First, background light (e.g room light and laser scatter) was subtracted from each experimental spectrum. The background subtracted spectra were then filtered to remove shots that did not contain the N_2 fundamental vibrational mode due to excessive laser scatter. Additionally, experimental parameters such as probe bandwidth, chirp, pulse shape, and time delay; pump and Stokes bandwidth, chirp, and peak wavelength; and the detection instrument function were determined for every experiment and used to inform the development of a library of CARS spectra. The experimental frequency axis (in wavenumber) was determined, and a shift and resampling was applied to the numerical simulation to match the experimental axis as dictated by the spectrometer and camera resolution. To determine best fit temperatures, each experimental spectrum was then compared to the simulation database. The differential evolutionary algorithm was used to minimize the norm of the residuals between experiment and simulation. The current version of the fitting algorithm was allowed to vary the intensity scaling (a) to ensure proper normalization of the vector characterizing the experimental spectra ($\mathbf{d}$), the vertical shift (b) of the experimental spectrum as well as the temperature of the simulated spectra, s(T). The vector of residuals ($\mathbf{r}$) was calculated using these three parameters through Eq. 4.3

$$\mathbf{r} = a\mathbf{d} + b - \mathbf{s}(T) \tag{4.3}$$

The ℓ^2-norm of this vector was minimized by varying a, b, and T. The temperature of the simulated spectra that led to this minimization was recorded for each experimental spectra. These temperatures were then filtered to exclude fits that converge on the library limits (e.g. 900 K and 2800 K). The average temperature was then acquired through averaging the remaining best fit temperatures and the standard deviation from the average was reported.

4.3 Adiabatic Flame Validation

The fs/ps CARS technique was validated using a well-characterized H_2–air laminar diffusion flame stabilized over a Hencken burner. The discussion of how an adiabatic flame can be used to inform model parameters is given in Section 4.1.1

CARS measurements were made 3.81 cm above the Hencken burner surface at flow rates informed by Hancock et al [30]. To suppress contributions from non resonant background, a probe delay of $\tau =$ 5.1 ps was chosen for analyzing the spectral response of the flame while maintaining optimal signal levels. Additionally, a later probe delay of $\tau = 38.4$ ps for enhanced sensitivity at temperatures below ∼1000 K was also employed. Miller et al. [23] demonstrated the use of long probe delays to study low-temperature sensitivity from ground vibrational state ro-vibrational revivals. While not analyzed in this work, late probe delay spectra have been acquired for all flame conditions studied and may be used in the future.

After the spectral parameters from the H_2/air flame were evaluated, the spectral library was populated with simulated spectra for comparison with the experiment. The aforementioned differential evolutionary algorithm was used to determine the best-fit temperature for the experiment. In Fig. 4.3, a spectrum calculated at the average best fit temperature is compared to the average of 500 laser shots recorded at an equivalence ratio of ϕ=1.1. Good agreement is observed between the best fit temperature and experimental spectra.

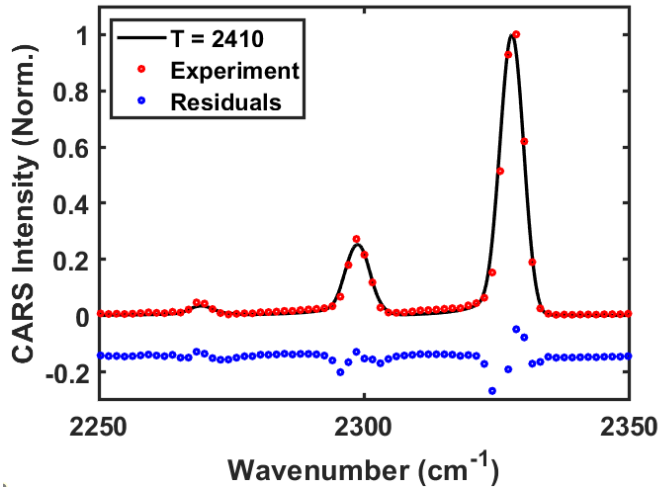

Figure 4.3: Average N_2 fs/ps vibrational CARS spectrum calculated from 500 laser shots recorded within the products of a $\phi = 1.1$ flame compared with simulation at 2410 K.

The adiabatic flame temperature and best fit temperatures using the early probe delay CARS spectra are plotted for a range of equivalence ratios in Fig. 4.4 to evaluate the accuracy of the

fs/ps CARS measurements. The error bars are used to denote one standard deviation of the best fit temperatures from 500 individual measurements. Two trends are apparent in Fig. 4.4. One is that the accuracy of the best fit temperatures increases with rising temperature, and the second is that the precision of these fits decrease with increasing temperature. Lower accuracy at low equivalence ratios is expected, however, the error in best-fit temperature for the spectra acquired at $\phi = 0.3$ exceeds the typical performance. Anticipated fs/ps performance over the temperature range fit here is ~98% [60] while the temperature fit at this equivalence ratio differs from the adiabatic temperature by ~160 K (14%). This is due to a failure in the current fitting routine to converge to lower temperatures. For the lower temperatures, the fitting routine does not converge on the correct answer and instead converges on a higher temperature shown in Fig. 4.5. This error in the temperature fitting routine will need to be addressed in future work for accurate measurements recorded near the low-temperature limit of fs/ps CARS sensitivity.

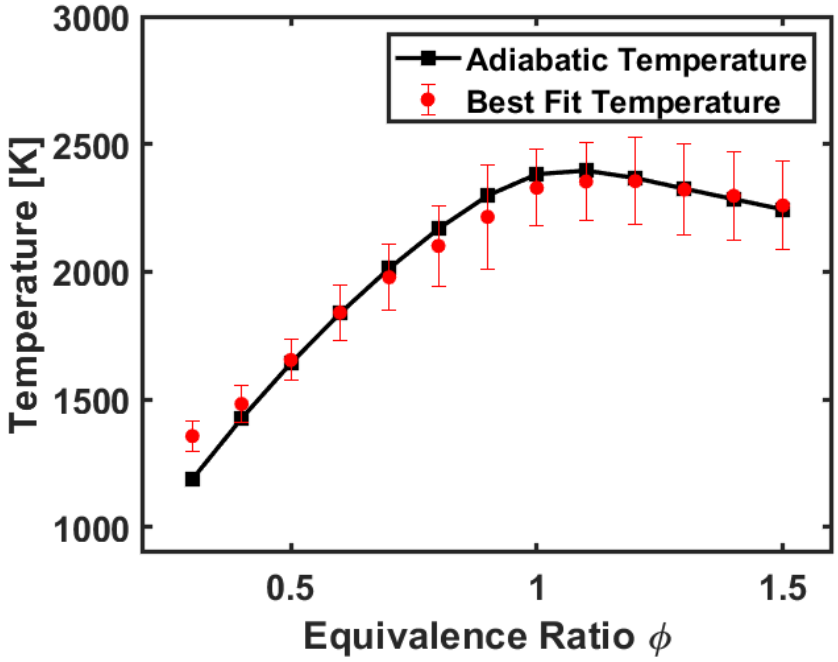

Figure 4.4: Measured temperatures recorded in the products of an adiabatic flame with best fit temperature and predicted adiabatic flame temperature shown for a range of equivalence ratios. Error bars represent one standard deviation of the best-fit temperature.

In contrast, the accuracy of the best fit temperature measurement made at ϕ=1.1 was within ~1.2% of the expected adiabatic flame temperature of 2396 K. This measurement does show a lower precision than low temperature results. Lower precision at higher temperatures can be attributed to the decreased signal intensity at low densities. This is observed by visually comparing single-shot

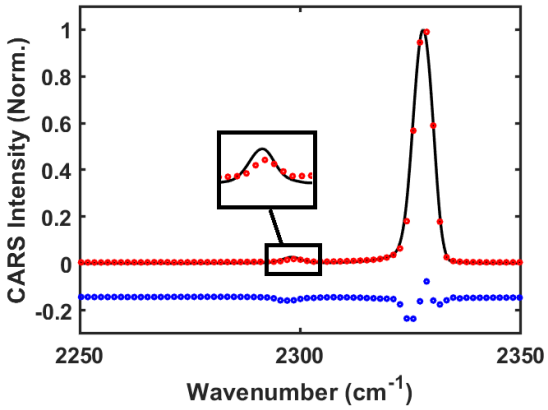

Figure 4.5: Best fit temperature of 1415K plotted with experimentally measured spectrum at an equivalence ratio of ϕ=0.3 and the residuals between the two. The experimental hotband is emphasized to show poor convergence of the fitting routine.

spectra for an equivalence ratio of $\phi = 0.3$ to that of the equivalence ratio of $\phi = 1.1$, shown in Fig. 4.7. As is shown by the residuals from the difference between the experimental and modeled spectra, the noise at the baseline is much greater for the spectra acquired at ϕ=1.1. This noise is used in the calculation of a signal-to-noise ratio (SNR) for each spectra. The SNR in this work has been calculated by dividing the maximum intensity of each spectra by the standard deviation of its baseline and taking the average of the result over 500 spectra.

$$SNR = \frac{I_{max}}{\sigma_{baseline}} \tag{4.4}$$

The result is shown in Fig. 4.6, where the trend of decreasing SNR with increasing temperature is apparent. The maximum SNR is measured for the spectra taken at the equivalence ratio of ϕ=0.3 whereas the mimimum occurs at ϕ=0.9 with an SNR of 27. However, on either side of the minima, SNR is > 30. Decreaasing SNR is expected as temperature increases because CARS signal intenstiy is approximately proportional to number density squared.

In summary, a spectral library informed by the parameters extracted from experimental spectra taken in an adiabatic flame has been developed. With the exception of spectra acquired at ϕ=0.3, best fit temperatures for experimental spectra have been shown to have good agreement with the adiabatic flame temperature. Two trends have been identified for the current fs/ps CARS system: accuracy trends proportionately with temperature, whereas precision trends inversely with temperature. The performance of the CARS system coupled with stable signal intensity during translation has demonstrated its suitability for further temperature measurements in the counterflow burner.

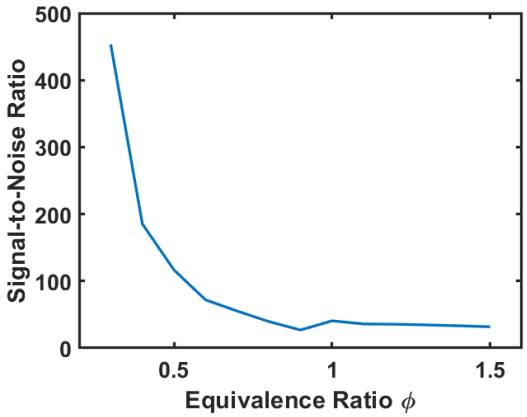

Figure 4.6: Average Signal-to-Noise ratio.

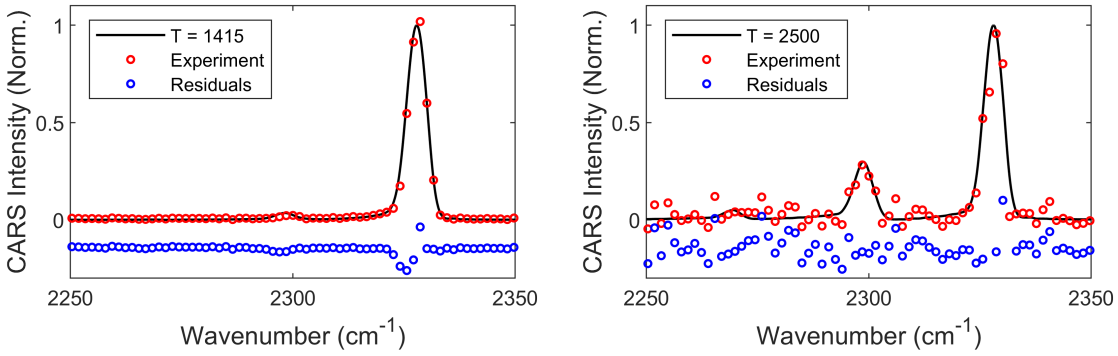

Figure 4.7: Single-shot N_2 fs/ps CARS for the best fit temperatures and fit residuals for equivalence ratios $\phi = 0.3$ and 1.1 at a) 1415 K and b) 2500 K respectively.

4.4 Flame Image Results

For each pressure and strain rate of interest, a series of 240 images of flame luminescence was acquired using a FLIR Chameleon 3 CMOS (image scale of 8.46 $\mu m/pix$) as detailed in Section 2.3. These images were used to characterize the stability of the reaction zone along the centerline. An example image is shown in Fig. 4.8. Laser scatter was used to illuminate the nozzles in the images. To determine the spatial location of the probe volume, the stages were translated vertically until scatter was observed on the nozzle to establish an upper and lower bounds. This leads to an uncertainty in measurements of axial location of ± 0.1 mm. The exposure time of 58.8 ms was insufficient to resolve the flame at its edges giving the edge fluctuations a fan-like appearance. The image was subsequently cropped horizontally to show only the centerline.

As can be seen in Fig. 4.9, the average axial position of the centerline changes with increasing pressure and strain rate. Increasing strain corresponds to a shift of the centerline closer to the fuel nozzle. The luminescence location was expected to inform the approximate location where the peak temperature will occur. This was used to identify a range of axial locations of interest for CARS measurements. This in turn allows expedited runs of the counterflow burner which becomes increasingly beneficial at higher pressures where the rate of fuel, oxidizer, and N_2 consumption increases. It can seen from Figure 4.9 that the stability of the flame location decreases as pressure increases. In particular, at a pressure of 4 atm and a theoretical strain rate of 500 1/s, the average position has the highest variance. This can be attributed to two sources. The first is the relatively low strain rate for the given pressure not constraining the stagnation plane, leading to an unstable flame. The other source is the presence of particles in the chamber that were difficult to completely remove. These include particle imaging velocimetry (PIV) particles that had been fed into the burner for a previous experiment. While less likely, the presence of particles could lead to disruptions in the flow field and lend to the instability observed.

In summary, stability of the flame's centerline and its relative spatial location within the counterflow burner was presented. Future improvements upon flame stability include purging the counterflow burner before operation to ensure minimal interference in the flow field. Additional improvements may seek to use more robust methods for characterizing spatial deviation with higher resolution, such as intensified high-speed imaging or OH planar laser induced fluorescence.

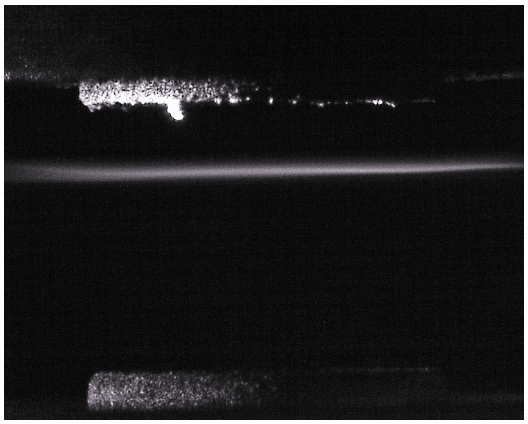

Figure 4.8: Example image recorded within the counterflow burner at 2.5atm and a theoretical strain rate of 450 1/s using an observation camera.

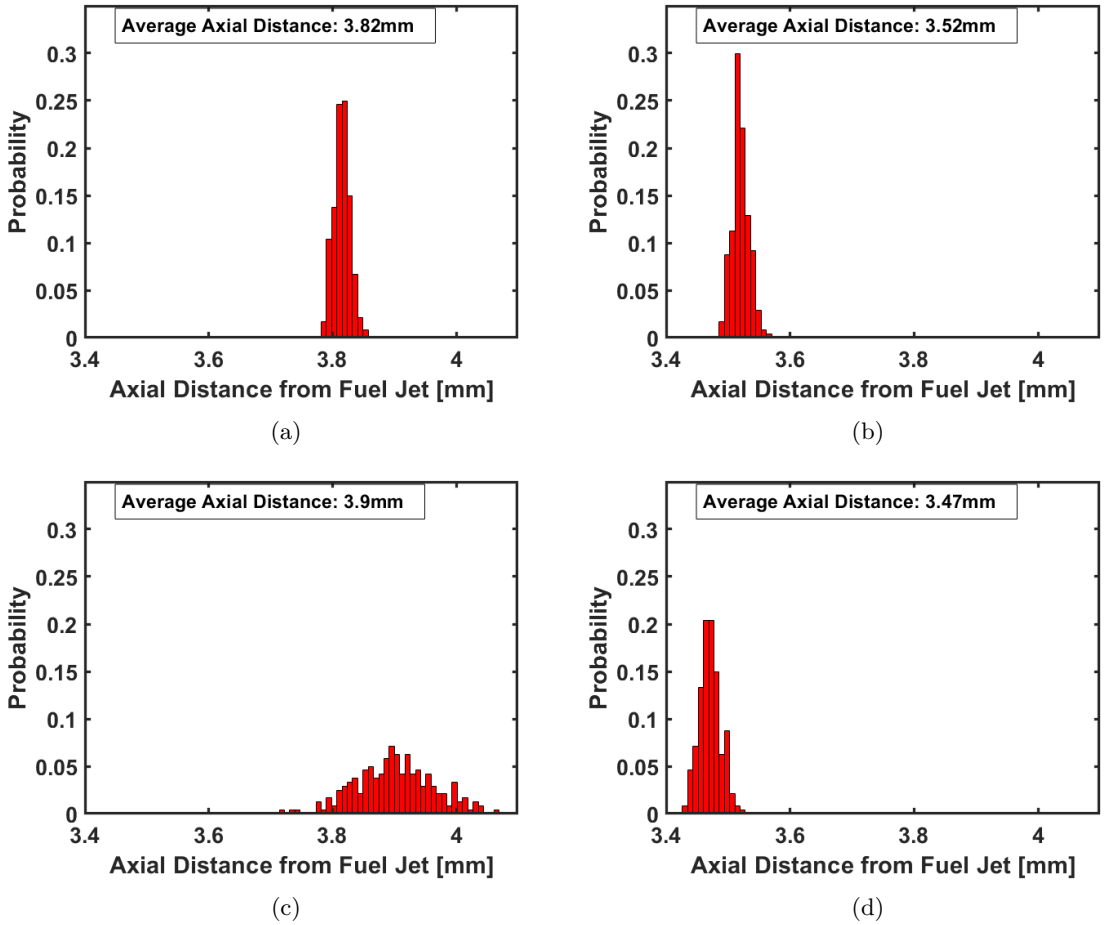

Figure 4.9: A histogram of the the axial location from the fuel jet where the maximum luminescence was detected by the FLIR camera for a)2.5atm and a theoretical strain rate of 450 1/s, b)2.5atm and a theoretical strain rate of 900 1/s, c)4atm and a theoretical strain rate of 500 1/s, d) 4atm and a theoretical strain rate of 1000 1/s.

4.5 Counterflow Flame Thermometry

4.5.1 Experimental Results: fs/ps CARS Spectra

Spectra acquired using vibrational fs/ps CARS are analyzed for temperature at pressures of 2.5 and 4 atm at low and near-extinction strain rates. The spectral fitting routine detailed in Section 4.2.1 was used to analyze the spectra acquired and minimize the residuals between the spectral library and experimental spectra to determine temperature. Spectra are acquired while conducting a vertical scan that translates the CARS probe volume from the oxidizer nozzle to the fuel nozzle. For the purpose of conserving fuel, each scan began 0.2 mm beyond the initial detection of the "hot band" ($N_2(V_2 \longrightarrow V_1)$). The probe pulse was delayed by 5.1 ps to minimize non-resonant contributions to the signal. Although not used for temperature determination in the current study, a secondary time delay of 38.4 ps was also captured in an attempt to heighten sensitivity to temperatures below 1100 K. For each axial position at each pressure and strain rate, 2000 single-laser-shot spectra were acquired at a kilohertz rate. For clarification of the language subsequently used, a "single-shot-spectrum" refers to a single spectrum pulled from the spectral series for a given position and condition.

Example single-shot spectra obtained at various axial locations within the counterflow burner are presented in Fig. 4.10. The top row corresponds to spectra obtained at a probe delay of 5.1 ps, whereas the bottom row corresponds to the late probe delay of 38.4 ps. By comparison, spectra shown in Fig. 4.11 consist of an average of the spectral series. These averages for each position are acquired by averaging a total of 500 arbitrarily chosen shots from the spectral series. 500 shots were chosen as it corresponded to the lowest number of remaining shots from across all spectral series acquired after the filtering routine was used to process the original 2000 shots. This was made relevant by the scan of the 4 atm and a theoretical strain rate of 1000 strain 1/s condition as there were several shots obtained at each position that were not able to be fit for temperature as will be explained later in this section.

While not explored at length in this work, it is important to note for future work that the same fs/ps CARS system can excite Raman transition for multiple species simultaneously to quantify relative species concentrations in addition to temperature. This can be seen in Fig. 4.12 with the appearance of another band near 2880 cm^{-1} which corresponds to Q-branch transitions of the CH_4 molecule.

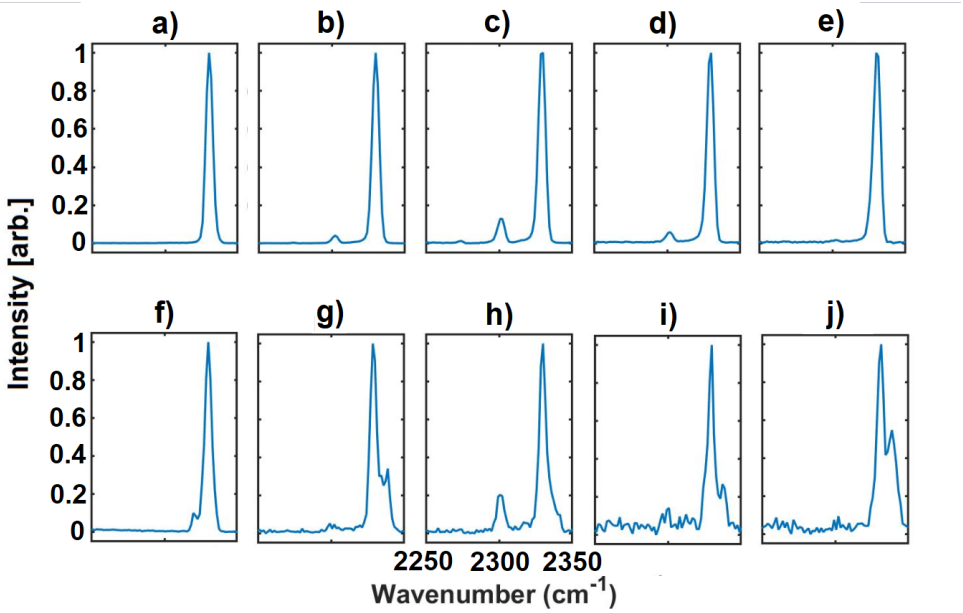

Figure 4.10: Single shot spectra obtained using an early probe delay, 5.1 ps (top row), and a late probe delay, 38.1 ps (bottom row), for a pressure of 2.5 atm and a theoretical strain rate of 450 1/s at axial locations of a,f) 4.3 mm b,g) 4.1 mm c,h) 3.9 mm d,i) 3.7 mm e,j) 3.5 mm.

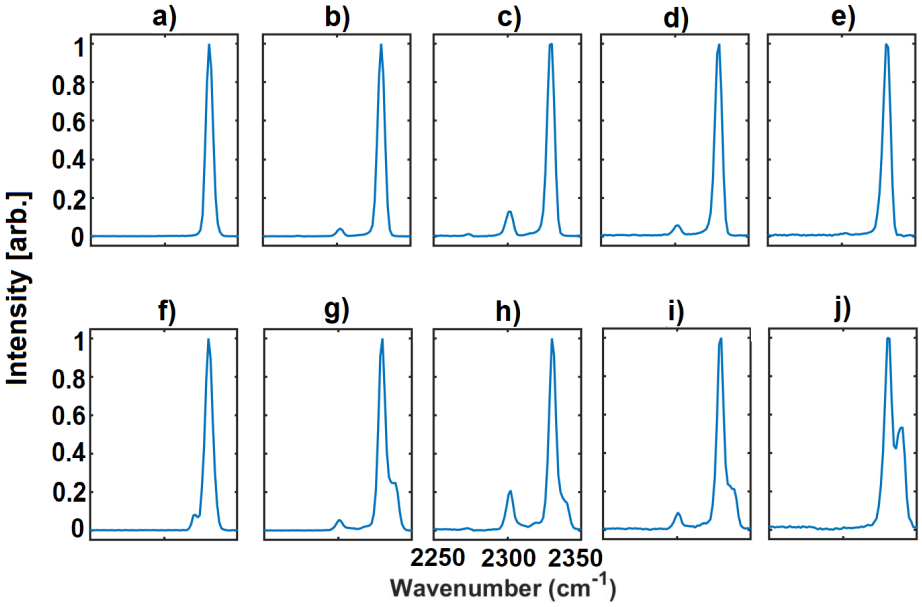

Figure 4.11: Averaged spectra from 500 laser shots shown for comparison relative to the single shot spectra in Fig. 4.10. Spectra obtained using an early probe delay (top row) and a late probe delay (bottom row) for a pressure of 2.5 atm and a theoretical strain rate of 450 1/s at axial locations of a,f) 4.3 mm b,g) 4.1 mm c,h) 3.9 mm d,i) 3.7 mm e,j) 3.5 mm.

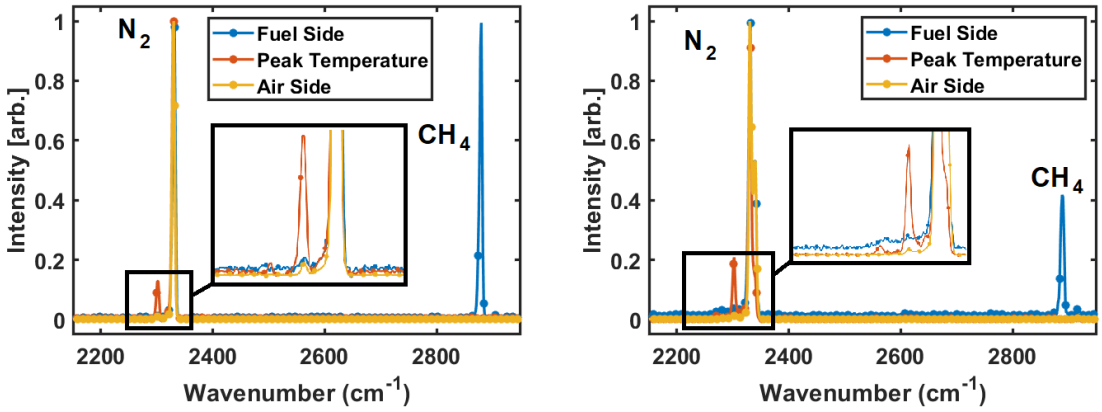

Figure 4.12: Overlapped spectra taken on either side of the flame and within the flame for both a) the early probe delay, and b) the late probe delay.

4.5.2 1D Flame Simulation Results

As stated previously, Cantera requires an input of fuel and oxidizer species and concentration, theoretical strain rate, and pressure to calculate species and temperature profiles. Example simulations at 4 atm are shown in Fig. 4.13. Fuel and oxidizer concentrations are shown to deplete at approximately equidistant axial locations of 2.725 mm from their respective nozzles as would be expected for balanced momentum fluxes for the given domain width of 5.45 mm. Maximum CH mole fraction occurs at the same axial location as the peak gas temperature. As a result, it is expected that the contribution from the chemiluminescence of CH to the flame's intensity visualized in Fig. 4.8 would align with the peak temperature. However, the flame emission detected by the camera is not filtered for CH chemiluminescence, so there are potentially other emissive species, such as OH, contributing to the flame emission observed.

Calculated temperature profiles at each experimental condition are compared against one another in Fig. 4.14 to visualize the approximate change in magnitude and location of the peak temperature expected when evaluating experimental temperature profiles. From this comparison it is expected that temperature will increase as a function of increasing pressure but decrease as a function of increasing strain rate, while axial distance from the fuel nozzle is primarily dependent on strain rate. Additionally, it is observed that the peak temperature at the lower strain rates occurs further from the fuel than the near-extinction strains. As Kang et al. [61] reported previously, counterflow diffusion flames featuring hydrocarbon fuels tend to form closer to the oxidizer inlet.To counteract this, either fuel dilution is required or, as has been observed through this experiment, an increase of the strain rate is required with both relying on fulfilling the criterion set by

$$\left[\frac{m_{0,0}/Le_{\mathrm{O}}^{1/2}}{m_{\mathrm{F},0}/Le_{\mathrm{F}}^{1/2}}\right] > i \tag{4.5}$$

where $\mathrm{m}_{O,0}$ is the free stream mass fraction of the oxidizer, $\mathrm{m}_{F,0}$ is the free stream mass fraction of the fuel, i is the mass stoichiometric coefficient, and Le is the appropriate Lewis number. In the case of an increase in strain rate, the stagnation plane itself is constrained leading to a thinner flame, reflected by its narrower temperature profile compared to that of lower strain rate flames, which in turn narrows the region within which the fuel molecules may diffuse.

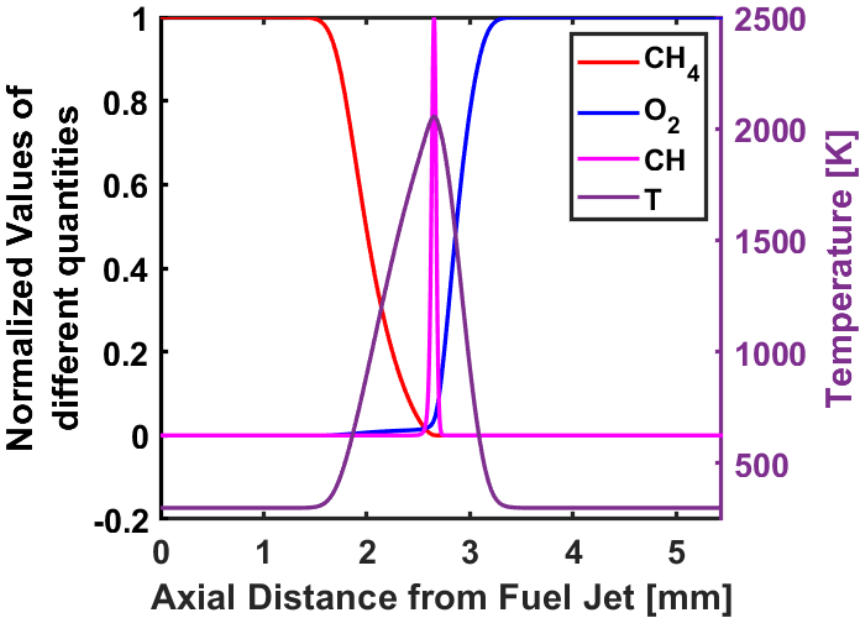

Figure 4.13: Cantera calculated normalized profiles for temperature and various species of interest plotted against axial distance from the fuel nozzle for a pressure of 4 atm and a theoretical strain rate of 1000 1/s.

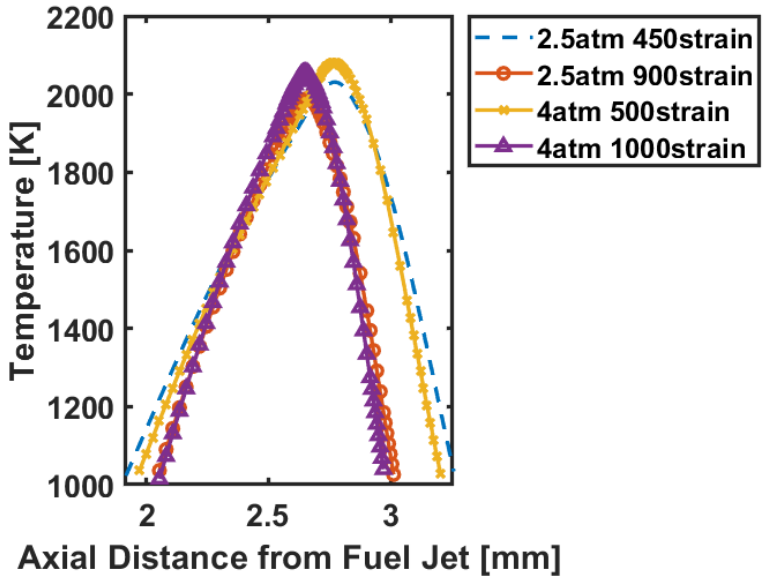

Figure 4.14: Plots comparing the Cantera calculated temperature plots for all acquired pressures and strain rates.

4.5.3 Experimental Results: Flame Temperature

A comparison of the Cantera-simulated temperature and best fit temperature profiles is shown in Fig. 4.15. Figure 4.15a shows both experimental and Cantera simulated temperature profiles at their actual axial locations, and Fig. 4.15b compares the two temperature profiles with the axial location of the Cantera profile offset to match that of the best-fit temperature.

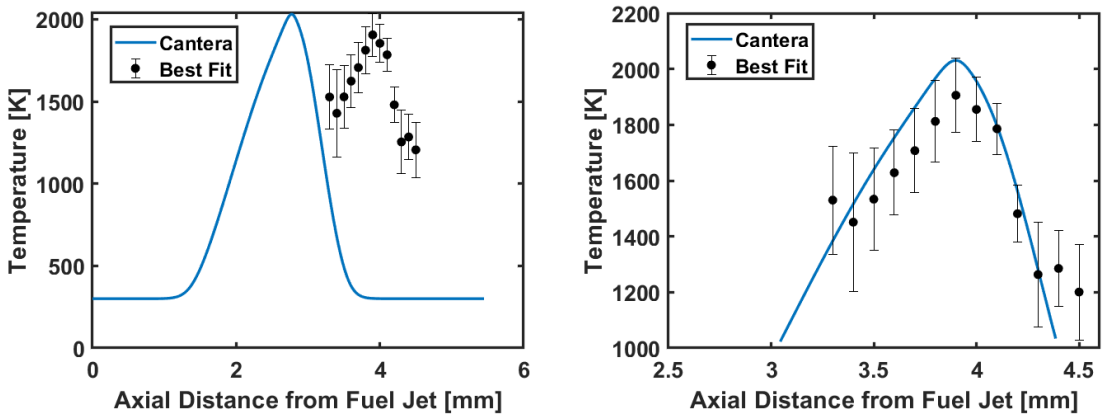

(a) (b)

Figure 4.15: Cantera calculated temperature and best-fit temperature with error bars of σ for 2.5 atm 450 strain 1/s at the axial locations a) calculated by Cantera and detected within the flame and b) offset to match that of Cantera for temperatures above 1000 K.

Although both temperature profiles peak closer to the oxidizer side, it can be observed that the spatial locations of the experimental temperature profile and that calculated by Cantera do not overlap. For the case of a pressure of 2.5 atm and a strain of 450 1/s, there is a 1.2 mm difference in peak temperature location. A potential cause for this offset may be due to a mismatch between the calculated stoichiometric mixing region and that achieved experimentally. While there exists a few differences between the experiment and the calculation, one potentially significant source of error may be the fuel and oxidizer mass flow controller accuracy at low flow rates. An improper flow rate would lead to an offset of the stagnation plane's location due to an improper balance of momentum. This may explain the degree of which the flame in this experiment was offset compared to Cantera predictions. Additionally, Cantera employs a similarity transformation to reduce the flow-field to a one-dimensional problem wherein the dependent variables of temperature and species mass fraction are functions of the axial direction only. This, in combination with not calculating diffusive fluxes, may also contribute to the offset between the Cantera and experimental temperature profiles. However, displacements of position between the flame calculation and the experiment have been observed previously by Satija [18] when observing counterflow flames with a fuel concentration

greater than 20%. No attempts to vary fuel dilution were made in this experiment, however, it is a point of interest for future experiments.

Because of the significant of offset between the simulations and the experiments, the calculation of axial position is treated as approximate. Future work could explore more advanced computational tools and investigate flow controller accuracy. Improved flow models with more accurate thermo-chemical properties will be required to accurately estimate extinction and provide further validity to the Cantera-calculated temperature profiles.

Regardless of the spatial offset, it can be seen in Fig. 4.15 that once the temperature profiles are overlapped in post-processing that there is reasonable agreement between the calculated Cantera temperature profile and the temperatures measured experimentally. The axial location offset between the calculated and measured flame profiles is observed for each of the pressure and strain conditions. However, for the strain rates near extinction the observed spatial offset between the calculated and experimental profiles decreases. There is a location difference of 1.2 mm at low theoretical strain rates compared to 0.8mm at high theoretical strain rates. This supports that one or both of the controllers are excessively inaccurate at low mass flow rates, i.e. lower strain rates, and improve with increasing flow rate. This would impact the thermal mixing layer and could lead to the flame position greatly differing from that of an ideal solution. To corroborate whether this is the source of error, the accuracy of mass flow controllers must be verified across the low flow rate range.

Shown in Fig. 4.16 is experimental data obtained for a pressure of 2.5 atm and a theoretical strain rate of 450 1/s. Figure 4.16(a) shows a histogram of the axial location of the maximum luminescent signal measured using the flame monitoring camera. The flame is observed to fluctuate with a standard deviation of 52 μm (1.37%). Therefore, with the resolution of the CARS measurement in the direction of temperature gradients (< 80 μm) for the given pressure and strain rate, the flame position fluctuations are sufficiently small enough for the purpose of evaluating peak temperature locations. Shown in Fig. 4.16c are experimental spectra with corresponding modeled spectra for best fit temperature acquired at the axial locations identified in Fig. 4.16b. As the best fit temperature does not change between Fig. 4.16c(left) and Fig. 4.16c(center), the axial location corresponding to the peak temperature is likely between 3.8 and 4.0 mm from the fuel nozzle. This supports the previous claim that flame emission images can inform the approximate location of peak temperature. Shown in Fig. 4.16d are spectra obtained at the later ps-probe delay. While these spectra are not fit for temperature, the spectral response from changing temperature can be visually observed through the ratio of the hot band to the fundamental vibrational mode. For example, it is seen that the

hot band in Fig. 4.16d(left) is of greater intensity than the one in Fig. 4.16d(right), which in turn corresponds to a higher temperature in Fig. 4.16d(left).

Seen in Fig. 4.17 are the calculated and experimental temperature profile plots for each pressure and strain rate explored. The best-fit temperature profiles are at the axial locations where they were observed experimentally, and the Cantera profiles were offset by the distance between the experimental and simulated peak temperatures. Each experimental condition tested has a temperature profile that approximates that of the Cantera calculation. The lower strain rates for both the calculation and the experiment exhibit a wider reaction region than the conditions near extinction, showcasing the constraint of the thermal mixing layer with increasing strain. However, also observable is that in all cases, there exists a low-temperature 'plateau' where CARS determined temperatures exceeds the expected temperature. This is caused by the failure of the spectral fitting routine at lower temperatures observed previously for the adiabatic flame measurements. Additionally, the Cantera-calculated profile is broader than the experimental profiles for each condition. This can in part be explained by a mismatch in ideal calculated chemical kinetics and applied experimental conditions. Another aspect that may be linked to this experimental mismatch is the significant standard deviation in best fit temperature observed. For each condition, the standard deviation in fit temperature exceeded the standard deviation for a comparable temperature fit for using the Hencken burner. This suggests an environmental factor impacting the experimental flame. One potential factor is the possibility that combustion products are recirculating into the reactant stream. This may happen if the reactant streams are turbulent causing unsteady diffusion of the products into the probe volume, or may occur if the products are not vented from the pressure chamber quickly enough. In future experiments, the use of planar laser induced fluorescence to track combustion intermediates and products as they are forced from the reaction zone could be employed. Another explanation may be derived from any radial mismatch between the two nozzles supplying the stream of reactants. If the flow fields are mismatched, not only are the strain rates observed not indicative of true near extinction strain rates, but could cause the flame to become increasingly unsteady. Although the flame's structure deviates near-extinction normally, misaligned reactant streams would cause greater variance near the center of the flame. However, this is less likely as the standard deviation of temperature remains highly variant away from the peak flame temperature. Particle imaging velocimetry could be used in the future to visualize the flow field and quantify gas velocity.

The error bars shown in Fig. 4.17 represent the standard deviation of the experimental temperature. The standard deviation of the peak temperature for each condition ranges is summarized in Tables 4.4, 4.5, 4.6, 4.7. The deviation in measured temperatures is larger than those observed for

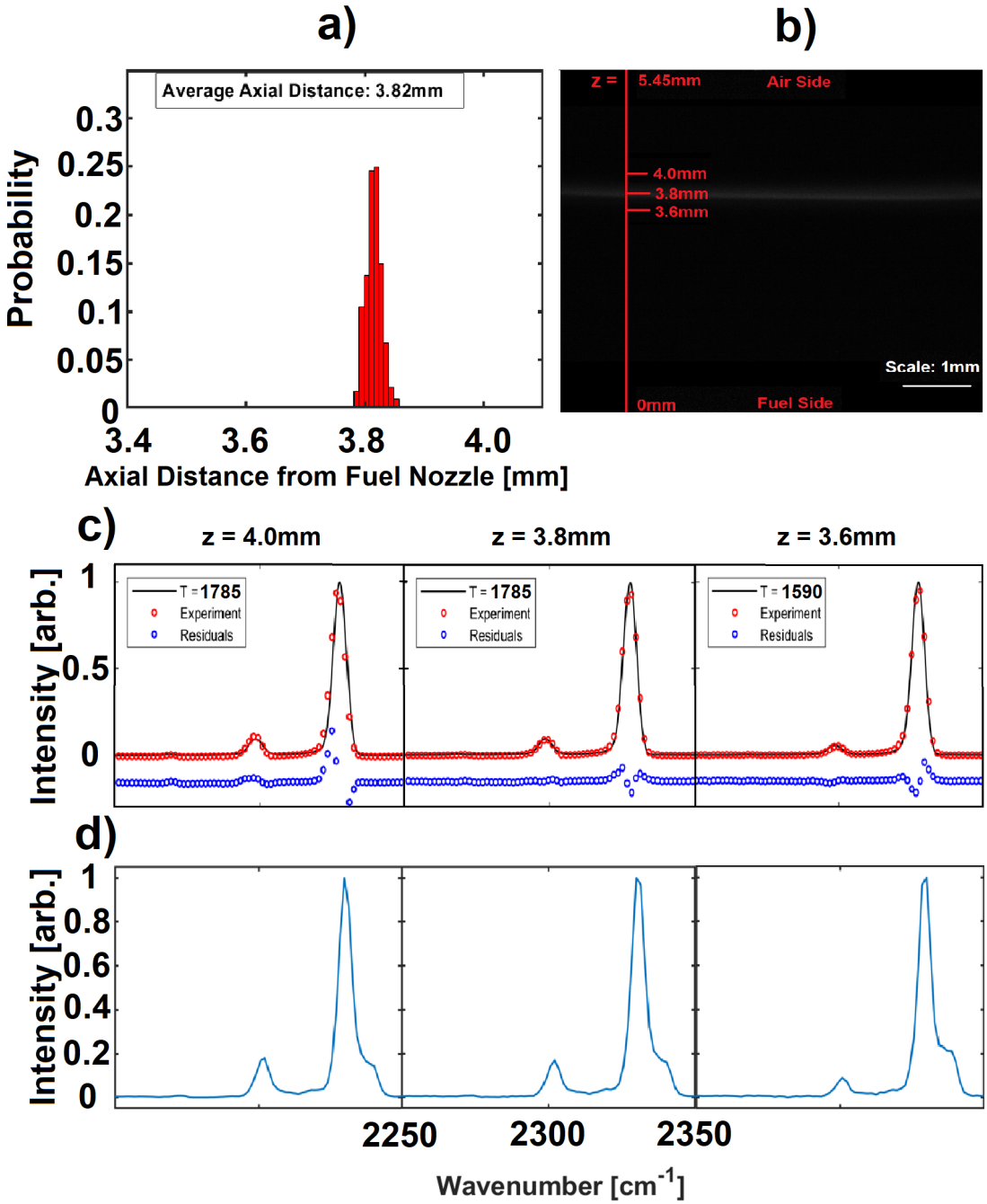

Figure 4.16: Results from the 2.5 atm, 450 1/s theoretical strain flame. a) A histogram of the the axial location relative to the fuel jet where the maximum luminescence was detected by the FLIR camera. b) Flame emission image with axial location markers centered around the average axial location from the histogram plot. c) Averaged CARS spectra shown with best-fit simulations measured at the axial locations from (b) with left to right corresponding to a distance from the fuel nozzle of 4.0mm, 3.8mm, and 3.6mm respectively. d) Averaged spectra for 500 shots taken for a late probe delay at the same axial locations as c) recorded in the same order.

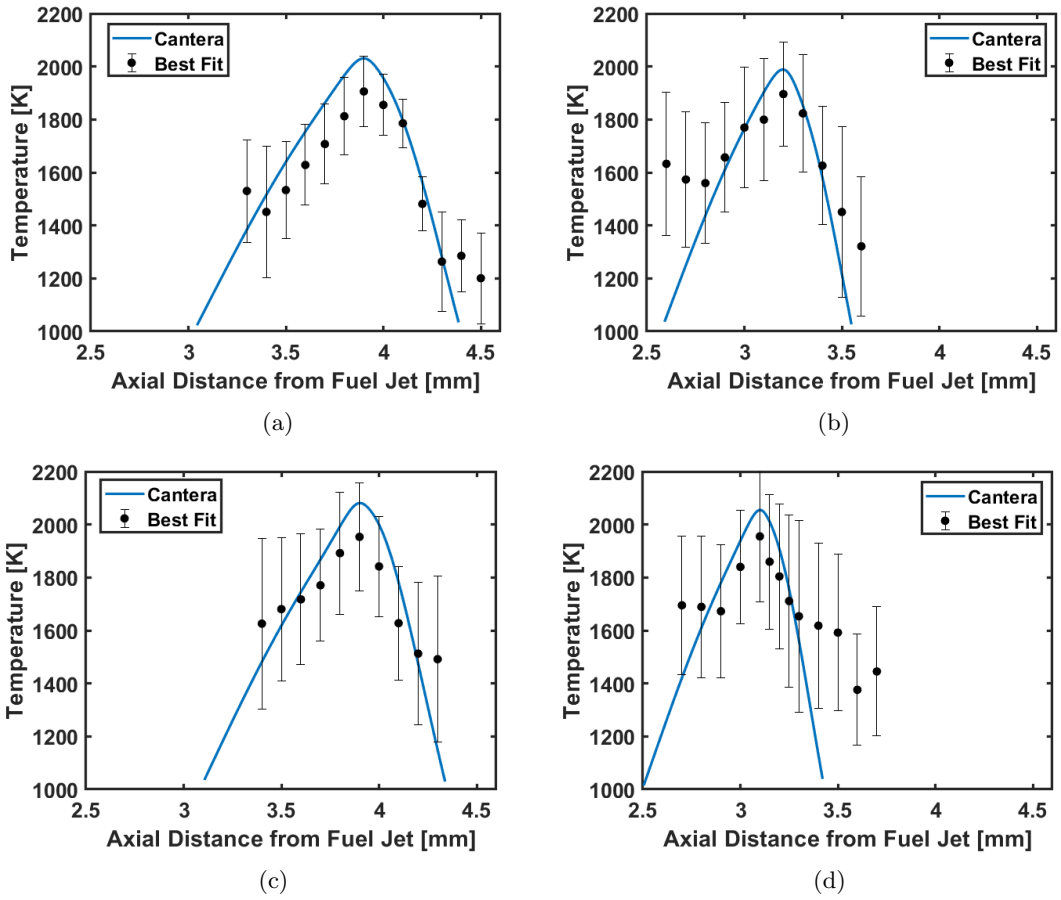

Figure 4.17: Best fit temperature profiles with spatial offset plotted against Cantera calculated temperature profiles for a) 2.5 atm 450 strain 1/s, b)2.5 atm 900 strain 1/s, c)4 atm 500 strain 1/s, and d) 4 atm 1000 strain 1/s.

the Hencken flame despite the maximum temperature not exceeding 2000 K. As has been investigated previously by Sarnacki [54], the turbulent Reynolds number, Re, in the current configuration is approximately 2600. While the primary flow of fuel and oxidizer were both within this limit with a maximum calculated Re of 2400, the N_2 coflow at the high strain conditions for both pressures approached or exceeded this limit with Re of 2500 and 2800 for the strain rates of 800 and 1000 1/s, respectively. This has the potential to cause beam steering as the measurement volume was propagated through the stagnation plane. If severe enough, beam steering can result in a spatial mismatch between the beams used for the CARS process thus leading to a reduction and loss of CARS signal. As the CARS signal intensity impacts the measurement precision, a varying probe volume could lead to greater variance in the best-fit temperatures derived from the spectral series acquired. Additionally, beam steering could cause transient fluctuations in the measurement volume location. Both effects could explain why the best fit temperature's standard deviation increases with

Table 4.4: Thermometry results near the peak flame temperature for low strain at 2.5 atm.

Pressure and Strain	Axial Location [mm]	$T_{Cantera}$	T_{Fit} [K]	T_{STD} [K], (%)	SNR
2.5 atm 450 strain	4.1	1771.94	1752.91	98.85 K (5.64%)	184.44
2.5 atm 450 strain	3.9	2030.89	1910.99	134.95 K (7.06%)	57.14
2.5 atm 450 strain	3.7	1864.16	1713.74	153.53 K (8.96%)	47.94

Table 4.5: Thermometry results near the peak flame temperature location for near extinction strain at 2.5 atm.

Pressure and Strain	Axial Location [mm]	$T_{Cantera}$	T_{Fit} [K]	T_{STD} [K], (%)	SNR
2.5 atm 900 strain	3.4	1541.61	1592.82	210.41 K (13.21%)	155.93
2.5 atm 900 strain	3.2	1988.65	1890.78	198.72 K (10.51%)	184.44
2.5 atm 900 strain	3.0	1767.37	1744.65	225.41 K (12.92%)	57.14

increasing strain rate. To verify this conclusion, further tests that focus on a single pressure for a range of strain rates would be necessary. Meanwhile, a spatial filter, as described in Chapter 2, was used to assist with blocking laser scatter from entering the spectrometer, however, the beams were still occasionally steered significantly resulting in signal contamination. This was most prevalent at the 4 atm with a theoretical strain rate of 1000 1/s case and led to many unusable shots due to the CARS signal overlapping pump scatter. Improvements to increase precision of the measurements are necessary for future application of fs/ps CARS to study high pressure combustion environments.

Although the precision of the measurements require significant improvement, good agreement is found between the calculated temperature profiles and the average temperature measured ex-

Table 4.6: Thermometry results near the peak flame temperature location for low strain at 4 atm.

Pressure and Strain	Axial Location [mm]	$T_{Cantera}$	T_{Fit} [K]	T_{STD} [K], (%)	SNR
4 atm 500 strain	4.1	1805.35	1652.69	214.68 K (12.99%)	155.93
4 atm 500 strain	3.9	2080.91	1968.35	211.79 K (10.76%)	184.44
4 atm 500 strain	3.7	1877.66	1781.91	220.42 K (12.37%)	57.14

Table 4.7: Thermometry results near the peak flame temperature location for near extinction strain at 4 atm.

Pressure and Strain	Axial Location [mm]	$T_{Cantera}$	T_{Fit} [K]	T_{STD} [K], (%)	SNR
4 atm 1000 strain	3.3	1569.53	1633.13	375.46 K (22.99%)	184.44
4 atm 1000 strain	3.1	2054.62	1975.92	239.68 K (12.13%)	47.94
4 atm 1000 strain	2.9	1804.35	1685.64	228.24 K (13.54%)	46.30

Table 4.8: Experimental temperatures and SNRs for the earlier reported Hencken burner results. Equivalence ratios shown correspond to temperatures measured within the counterflow burner.

Equivalence Ratio ϕ	$T_{adiabatic}$	T_{Fit} [K]	T_{STD} [K], (%)	SNR
0.4	1425	1463.82	69.82 K (4.77%)	185.32
0.5	1641	1641.8	81.43 K (4.96%)	116.53
0.6	1837	1827.25	99.40 K (5.44%)	71.82
0.7	2013	1980.08	132.07 K (6.67%)	55.15
0.7*	2013	2025.96	119.12 K (5.88%)	55.15

perimentally. The best fit peak temperatures were within 6% of the calculated peak temperatures with the lower strain rates corresponding to a ∼6% difference from the calculation and the elevated strain rates having an error of ∼4%. However, for the temperature range observed in the best fit temperature profiles, an accuracy of greater than 2% is expected based on measurements within the Hencken burner as shown in Table 4.8. This suggests that the experimental uncertainty is due to the burner environment. Of the three sources of uncertainty, the fuel and oxidizer flow rates and effects of beam steering, beam steering is least likely to influence the accuracy. It is more probable that the flow rates of one or both of the jets is generating a different flame condition than that being modeled. Additional work in characterizing the uncertainty in flame condition for the conditions explored in this experiment are required before a more direct conclusion can be made. For future improvements, a solution to remedy pump scatter rendering spectra unusable for temperature fitting must be made.

In summary, spectra obtained using hybrid fs/ps CARS within a counterflow geometry at two pressures and theoretical strain rates have been fit for temperature and compared with a calculated profile for temperature. Increasing pressure has been shown to lead to an increasing temperature,

whereas temperature decreases as the flame is evaluated at near extinction strain rates. Good agreement has been found between the calculated and best fit temperature profiles with 4-6% differences between the peak temperatures. Improvement of precision necessitates mitigating the effects of beam steering for maintaining good shot-to-shot standard deviation.

Chapter 5

Summary and Future Work

5.1 Summary

The characterization of well-controlled lab scale flames can be used to inform models that further our understanding of combustion processes. This study utilized a counterflow burner housed within a high-pressure chamber to generate laminar diffusion flames at pressures of 2.5 atm and 4 atm for theoretical strain rates far from and nearing extinction limits. Hybrid fs/ps CAR has been employed to quantify gas-phase temperature at atmospheric and elevated pressures. Resultant experimental CARS spectra were compared to theoretical simulations to determine *in-situ* gas temperature. A probe pulse model has been developed to simulate the experimental ps pulse generated using a folded 4-f pulse shaper. Temperature profiles derived from fitting the spectra taken within a near-adiabatic flame informed spectral parameters used in the analysis of spectra taken within the counterflow burner. The accuracy of the fs/ps CARS system in an adiabatic flame at the peak temperature was determined to be $\sim$1.2%. Temperature profiles obtained from spectra collected in the counterflow flame have been compared to computational 1D flame simulations. The fit temperature profiles were observed to be within a 6% margin of the calculated profiles.

The impact of the lab environment on the stability of the CARS system has been reported and sources of instability were mitigated. Efforts made to minimize the spatial drift of the laser beams over long distances have proven effective in ensuring long term system stability. Methods used to align fs/ps CARS have also been reported and the fs/ps CARS system was demonstrated as stable over the range of travel within the counterflow burner.

5.2 Future Work

The current fs/ps CARS system has been demonstrated for measurements in a high-pressure counterflow burner. Sources of instability in the system have been investigated and eliminated, enabling future measurements in larger combustion facilities.

Future improvements may seek to explore a larger range of pressures and global strain rates for a better characterization of the accuracy and precision of fs/ps CARS measurements in this application. Methods to improve the accuracy and precision of the temperature measurement should be explored, alongside a comparison of best fit temperature profiles to other simulation methods. To improve SNR, the alignment of the 4-f pulse shaper must be optimized, or replaced with another pulse shaping mechanism to utilize higher-energy probe pulses. Extending the fs/ps CARS system to enable quantitative one-dimensional single-pulse temperature measurements will allow for measurements to be made across the entire domain without the need to scan vertically, enabling single-shot measurements of temperature gradients and overcoming uncertainty in peak flame temperature due to fluctuations in flame position.

References

[1] Brendyn G. Sarnacki and Harsha K. Chelliah. Sooting limits of non-premixed counterflow ethylene/oxygen/inert flames using lii: Effects of flow strain rate and pressure (up to 30 atm). *Combustion and Flame*, 195:267–281, 2018.

[2] Frequently asked questions (faqs) - u.s. energy information administration (eia). Mar 2021. published by: U.S Energy Information Administration, Accessed: 2021-08-21.

[3] Importance of methane. published by: Environmental Protection Agency, Accessed: 2021-08-21.

[4] Chloe Dedic. Hybrid fs/ps coherent anti-stokes raman scattering for multiparameter measurements of combustion and nonequilibrium. 2017.

[5] Clayton Geipel. High-spatial-resolution laser diagnostics for a dual-mode scramjet. 2020.

[6] Alan C. Eckbreth. Boxcars: Crossed-beam phase-matched cars generation in gases. *Applied Physics Letters*, 32(7):421–423, 1978.

[7] Aman Satija, Shenli Yuan, and Robert P. Lucht. *Development of Combined Dual-Pump Vibrational and Pure-Rotational Coherent Anti-Stokes Raman Scattering (DPVCARS and PRCARS) Systems and their Application to Laminar Counter-flow Flames.*

[8] Ji Yu and Hua Meng. A numerical study of counterflow diffusion flames of methane/air at various pressures. *Science China Technological Sciences*, 57(3):615–624, Mar 2014.

[9] C.J. Sung, J.B. Liu, and C.K. Law. Structural response of counterflow diffusion flames to strain rate variations. *Combustion and Flame*, 102(4):481–492, 1995.

[10] Thomas Fiala and Thomas Sattelmayer. Nonpremixed counterflow flames: Scaling rules for batch simulations. *Journal of Combustion*, 2014:484372, Jun 2014.

[11] Gersten K. Schlichting (Deceased) H. *Exact Solutions of the Navier–Stokes Equations. In: Boundary-Layer Theory.* Springer, Berlin, Heidelberg, 2017.

[12] Francesco Carbone, Kevin Gleason, and Alessandro Gomez. Pressure effects on incipiently sooting partially premixed counterflow flames of ethylene. *Proceedings of the Combustion Institute*, 36(1):1395–1402, 2017.

[13] B.G. Sarnacki, G. Esposito, R.H. Krauss, and H.K. Chelliah. Extinction limits and associated uncertainties of nonpremixed counterflow flames of methane, ethylene, propylene and n-butane in air. *Combustion and Flame*, 159(3):1026–1043, 2012.

[14] Jun'ichi Sato. Extinction of counterflow diffusion flame in high pressures. *Combustion Science and Technology*, 75(1-3):103–113, 1991.

[15] J. G. Quintiere and A. S. Rangwala. A theory for flame extinction based on flame temperature. *Fire and Materials*, 28(5):387–402, 2004.

[16] Irvin Glassman and Richard A. Yetter. Chapter 2 - chemical kinetics. In Irvin Glassman and Richard A. Yetter, editors, *Combustion (Fourth Edition)*, pages 1–74. Academic Press, Burlington, fourth edition edition, 2008.

[17] T. Dreier, B. Lange, J. Wolfrum, M. Zahn, F. Behrendt, and J. Warnatz. Cars measurements and computations of the structure of laminar stagnation-point methane-air counterflow diffusion flames. *Symposium (International) on Combustion*, 21(1):1729–1736, 1988. Twenty-First Symposuim (International on Combustion).

[18] Aman Satija. Development and application of coherent anti-stokes raman scattering systems in reacting flows. 2013.

[19] A C Eckbreth. Laser diagnostics for combustion temperature and species. 1 1987.

[20] Francois M. Kamga and Mark G. Sceats. Pulse-sequenced coherent anti-stokes raman scattering spectroscopy: a method for suppression of the nonresonant background. *Opt. Lett.*, 5(3):126–128, Mar 1980.

[21] W. M. Tolles and R. D. Turner. A comparative analysis of the analytical capabilities of coherent anti-stokes raman spectroscopy (cars) relative to raman scattering and absorption spectroscopy. *Appl. Spectrosc.*, 31(2):96–103, Mar 1977.

[22] R. F. Begley, A. B. Harvey, and R. L. Byer. Coherent anti-stokes raman spectroscopy. *Applied Physics Letters*, 25(7):387–390, 1974.

[23] Joseph D. Miller, Chloe E. Dedic, and Terrence R. Meyer. Vibrational femtosecond/picosecond coherent anti-stokes raman scattering with enhanced temperature sensitivity for flame thermometry from 300 to 2400 k. *Journal of Raman Spectroscopy*, 46(8):702–707, 2015.

[24] Sukesh Roy, Terrence R Meyer, Robert P Lucht, Vincent M Belovich, Edwin Corporan, and James R Gord. Temperature and co2 concentration measurements in the exhaust stream of a liquid-fueled combustor using dual-pump coherent anti-stokes raman scattering (cars) spectroscopy. *Combustion and Flame*, 138(3):273–284, 2004.

[25] Sean P. Kearney. Hybrid fs/ps rotational cars temperature and oxygen measurements in the product gases of canonical flat flames. *Combustion and Flame*, 162(5):1748–1758, 2015.

[26] D. Romanov, A. Filin, R. Compton, and R. Levis. Phase matching in femtosecond boxcars. *Opt. Lett.*, 32(21):3161–3163, Nov 2007.

[27] Mikhail N. Slipchenko and Ji-Xin Cheng. *Nonlinear Raman Spectroscopy: Coherent Anti-Stokes Raman Scattering (CARS)*, pages 1744–1750. Springer Berlin Heidelberg, Berlin, Heidelberg, 2013.

[28] Andrew D. Cutler, Gaetano Magnotti, Luca Cantu, Emanuela Gallo, Robert Rockwell, and Christopher Goyne. Dual-pump coherent anti-stokes raman spectroscopy measurements in a dual-mode scramjet. *Journal of Propulsion and Power*, 30(3):539–549, 2014.

[29] Thomas Seeger and Alfred Leipertz. Experimental comparison of single-shot broadband vibrational and dual-broadband pure rotational coherent anti-stokes raman scattering in hot air. *Appl. Opt.*, 35(15):2665–2671, May 1996.

[30] Robert D. Hancock, Kenneth E. Bertagnolli, and Robert P. Lucht. Nitrogen and hydrogen cars temperature measurements in a hydrogen/air flame using a near-adiabatic flat-flame burner. *Combustion and Flame*, 109(3):323–331, 1997.

[31] ALAN C. ECKBRETH and ROBERT J. HALL. Cars concentration sensitivity with and without nonresonant background suppression. *Combustion Science and Technology*, 25(5-6):175–192, 1981.

[32] M. J. Cottereau, F. Grisch, and J. J. Marie. Cars measurements of temperature and species concentrations in an ic engine. *Applied Physics B*, 51(1):63–66, Jul 1990.

[33] R. L. Farrow, R. P. Lucht, and L. A. Rahn. Measurements of the nonresonant third-order susceptibilities of gases using coherent anti-stokes raman spectroscopy. *J. Opt. Soc. Am. B*, 4(8):1241–1246, Aug 1987.

[34] Robert P. Lucht, Paul J. Kinnius, Sukesh Roy, and James R. Gord. Theory of femtosecond coherent anti-stokes raman scattering spectroscopy of gas-phase transitions. *The Journal of Chemical Physics*, 127(4):044316, 2007.

[35] Sean Patrick Kearney. Bandwidth optimization of femtosecond pure-rotational coherent anti-stokes raman scattering by pump/stokes spectral focusing. 53(28), 7 2014.

[36] Terrence R. Meyer, Sukesh Roy, and James R. Gord. Improving signal-to-interference ratio in rich hydrocarbon—air flames using picosecond coherent anti-stokes raman scattering. *Applied Spectroscopy*, 61(11):1135–1140, 2007.

[37] Sukesh Roy, Terrence R. Meyer, and James R. Gord. Time-resolved dynamics of resonant and nonresonant broadband picosecond coherent anti-stokes raman scattering signals. *Applied Physics Letters*, 87(26):264103, 2005.

[38] Christopher J. Kliewer, Yi Gao, Thomas Seeger, Johannes Kiefer, Brian D. Patterson, and Thomas B. Settersten. Picosecond time-resolved pure-rotational coherent anti-stokes raman spectroscopy in sooting flames. *Proceedings of the Combustion Institute*, 33(1):831–838, 2011.

[39] Waruna D. Kulatilaka, Paul S. Hsu, Hans U. Stauffer, James R. Gord, and Sukesh Roy. Direct measurement of rotationally resolved h2 q-branch raman coherence lifetimes using time-resolved picosecond coherent anti-stokes raman scattering. *Applied Physics Letters*, 97(8):081112, 2010.

[40] Sukesh Roy, Daniel Richardson, Paul J. Kinnius, Robert P. Lucht, and James R. Gord. Effects of n2–co polarization beating on femtosecond coherent anti-stokes raman scattering spectroscopy of n2. *Applied Physics Letters*, 94(14):144101, 2009.

[41] Waruna Kulatilaka, J. Gord, and S. Roy. Effects of o 2 –co 2 polarization beating on femtosecond coherent anti-stokes raman scattering (fs-cars) spectroscopy of o 2. *Applied Physics B-lasers and Optics - APPL PHYS B-LASERS OPT*, 102:141–147, 09 2011.

[42] Benjamin D. Prince, Abhijit Chakraborty, Beth M. Prince, and Hans U. Stauffer. Development of simultaneous frequency- and time-resolved coherent anti-stokes raman scattering for ultrafast detection of molecular raman spectra. *The Journal of Chemical Physics*, 125(4):044502, 2006.

[43] Benjamin Douglas Prince. Development and application of a hybrid femtosecond/picosecond coherent raman probe designed for study of excited state systems. 2008.

[44] Miller J. D., Slipchenko M. N., Meyer T. R., Stauffer H. U., and Gord J. R. Hybrid femtosecond/picosecond coherent anti-stokes raman scattering for high-speed gas-phase thermometry. *Optics Letters*, 35(14):2430–2432, 2010.

[45] Clayton M. Geipel, Andreas H. Rauch, H. Chelliah, and Chloe E. Dedic. Hybrid fs/ps cars system for counterflow flame investigation. 2020.

[46] Chloe Dedic, Andrew D. Cutler, and Paul M. Danehy. Characterization of supersonic flows using hybrid fs/ps cars. In *AIAA Scitech 2019 Forum*, 2015.

[47] Joseph Daniel Miller. Hybrid femtosecond/picosecond coherent anti-stokes raman scattering for gas-phase temperature measurements. 2012.

[48] Hans U. Stauffer, Joseph D. Miller, Mikhail N. Slipchenko, Terrence R. Meyer, Benjamin D. Prince, Sukesh Roy, and James R. Gord. Time- and frequency-dependent model of time-resolved coherent anti-stokes raman scattering (cars) with a picosecond-duration probe pulse. *The Journal of Chemical Physics*, 140(2):024316, 2014.

[49] Joseph D. Miller, Chloe E. Dedic, Sukesh Roy, James R. Gord, and Terrence R. Meyer. Interference-free gas-phase thermometry at elevated pressure using hybrid femtosecond/picosecond rotational coherent anti-stokes raman scattering. *Opt. Express*, 20(5):5003–5010, Feb 2012.

[50] Hans U. Stauffer, K. Arafat Rahman, Mikhail N. Slipchenko, Sukesh Roy, James R. Gord, and Terrence R. Meyer. Interference-free hybrid fs/ps vibrational cars thermometry in high-pressure flames. *Opt. Lett.*, 43(20):4911–4914, Oct 2018.

[51] Christain Brackmann, Joakim Bood, Marcus Alden, Gaelle Pengloan, and Olivind Andersson. Quantitative measurements of species and temperature in a dme-air counterflow diffusion flame using laser diagnostic methods. *Combustion Science and Technology*, 178(6):1165–1184, 2006.

[52] N Chai, W Kulatilaka, S Naik, N Laurendeau, R Lucht, R Kuehner, S Roy, V Katta, and J Gord. Nitric oxide concentration measurements in atmospheric pressure flames using electronic-resonance-enhanced coherent anti-stokes raman scattering. *Appl. Phys. B*, 88:141–150, 2007.

[53] Aman Satija, Xianan Huang, Pratikash P. Panda, and Robert P. Lucht. Vibrational cars thermometry and one-dimensional simulations in laminar h2/air counter-flow diffusion flames. *International Journal of Hydrogen Energy*, 40(33):10662–10672, 2015.

[54] Brendyn Sarnacki. Pressure and flow residence time effects on soot properties in counterflow non-premixed hydrocarbon-air flames. 2014.

[55] C. E. Dedic, T. R. Meyer, and J. B. Michael. Single-shot ultrafast coherent antistokes raman scattering of vibrational/rotational nonequilibrium. *Optica*, 4(5), 2017.

[56] Gregory P. Smith, David M. Golden, Michael Frenklach, Nigel W. Moriarty, Boris Eiteneer, Mikhail Goldenberg, C. Thomas Bowman, Ronald K. Hanson, Soonho Song, William C. Gardiner Jr., Vitali V. Lissianski, and Zhiwei Qin. Gri-mech 3.0. *http* : $//www.me.berkeley.edu/gri_mech/$.

[57] Joseph D. Miller, Mikhail N. Slipchenko, Terrence R. Meyer, Hans U. Stauffer, and James R. Gord. Hybrid femtosecond/picosecond coherent anti-stokes raman scattering for high-speed gas-phase thermometry. *Opt. Lett.*, 35(14):2430–2432, Jul 2010.

[58] Joseph D. Miller, Mikhail N. Slipchenko, and Terrence R. Meyer. Probe-pulse optimization for nonresonant suppression in hybrid fs/ps coherent anti-stokes raman scattering at high temperature. *Opt. Express*, 19(14):13326–13333, Jul 2011.

[59] Rammohan Mallipeddi and Ponnuthurai Nagaratnam Suganthan. Differential evolution algorithm with ensemble of parameters and mutation and crossover strategies. In Bijaya Ketan Panigrahi, Swagatam Das, Ponnuthurai Nagaratnam Suganthan, and Subhransu Sekhar Dash, editors, *Swarm, Evolutionary, and Memetic Computing*, pages 71–78, Berlin, Heidelberg, 2010. Springer Berlin Heidelberg.

[60] Chloe E. Dedic, Joseph D. Miller, and Terrence R. Meyer. Dual-pump vibrational/rotational femtosecond/picosecond coherent anti-stokes raman scattering temperature and species measurements. *Opt. Lett.*, 39(23):6608–6611, Dec 2014.

[61] K.T. Kang, J.Y. Hwang, S.H. Chung, and W. Lee. Soot zone structure and sooting limit in diffusion flames: Comparison of counterflow and co-flow flames. *Combustion and Flame*, 109(1):266–281, 1997.